

## Semiconductor photothermal materials enabling efficient solar steam generation toward desalination and wastewater treatment

Idris Ibrahim <sup>a</sup>, Dong Han Seo <sup>a</sup>, Andrew M. McDonagh <sup>b</sup>, Ho Kyong Shon <sup>a</sup>, Leonard Tijing <sup>a,\*</sup>

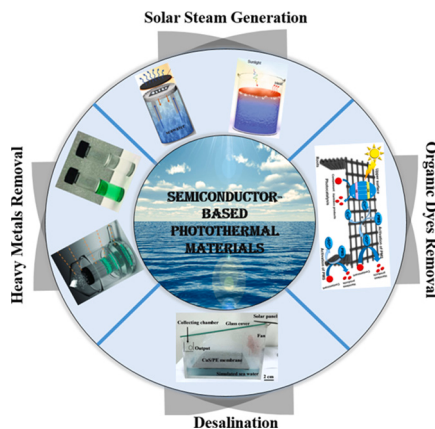
<sup>a</sup> Centre for Technology in Water and Wastewater, School of Civil and Environmental Engineering, University of Technology Sydney, PO Box 123, 15 Broadway, Sydney, NSW 2007, Australia

<sup>b</sup> School of Mathematical and Physical Sciences, University of Technology Sydney, PO Box 123, 15 Broadway, Sydney, NSW 2007, Australia

### HIGHLIGHTS

- Semiconductor-based photothermal materials are desirable for solar steam generation.
- This review highlights their mechanisms, designs and application in desalination.
- Knowledge gaps and further research needed are laid out.

### GRAPHICAL ABSTRACT



### ARTICLE INFO

**Keywords:**  
Semiconductors  
Photothermal materials  
Solar steam generation  
Water purification  
Desalination

### ABSTRACT

Water scarcity issues around the world have renewed interest in the use of solar water evaporation as a means of providing fresh water. Advances in photothermal materials and thermal management, together with new interfacial system designs, have considerably improved the overall efficiency of solar steam generation (SSG) for desalination and wastewater treatment. Several classes of rationally-designed photothermal materials (PTMs) and nanostructures have enabled effective absorption of broad solar spectrum resulting in improved solar evaporation efficiency. Among several classes of PTMs, semiconductor-based PTMs have demonstrated great potential for SSG. In this review, we highlight the progress and prospects in SSG with emphasis on the use and evolution of advanced semiconductor materials for PTMs and their various designs and engineered architectures. Applications and future prospects for desalination and wastewater treatment are also discussed.

\* Corresponding author.

E-mail address: [leonard.tijing@uts.edu.au](mailto:leonard.tijing@uts.edu.au) (L. Tijing).

## 1. Introduction

It is forecast that by 2050 around four billion people will be affected by freshwater scarcity due to rising population and industrialization [1]. Almost 80% of human diseases result from unsafe water and sanitation [2], therefore, improving water quality is necessary to enhance the general well-being of the population. Seawater desalination processes are reliable technologies that meet the growing demand for freshwater. Global desalination capacity is currently  $\sim 70$  million  $\text{m}^3\text{day}^{-1}$  and is increasing [3]. Highly efficient thermally-driven desalination technologies are used such as multi-stage flash (MSF) and multi-effect desalination (MED), but they are still economically and geographically impractical for small-scale applications [4]. Pressure-driven membrane desalination processes, such as seawater reverse osmosis (RO) technology currently dominate the desalination market due to simple operation, ability to produce high-purity water, low upfront capital investment and operating costs compared to thermally driven processes [5]. However, concentration polarization effects limit the overall water recovery of RO to less than 50% and reduce energy efficiency in further recovery of water [6]. Additionally, RO membranes require frequent cleaning or replacement due to scaling and fouling phenomena, which increases the operation costs.

Wastewater treatment (mainly that generated by industry) is another important source of freshwater. A widely adopted technology for wastewater treatment uses activated carbon adsorbents, where pollutants are adsorbed by the active material for removal. Common adsorbent materials exhibit some drawbacks which limit their applications, including inadequate removal of hydrophilic micropollutants, slow pollutant uptake, and challenges in regenerating the absorbent [7]. Therefore, it is desirable to develop advanced, renewable and sustainable technologies for clean water production to mitigate the ever-increasing global demand for clean water and energy consumption.

An alternative renewable energy-driven, sustainable clean water production process is solar-driven water evaporation, also known as solar steam generation (SSG). SSG utilizes sunlight to evaporate water and then condenses it to high purity water [3,8–15]. This technology has potential in industrial wastewater purification as well as water desalination with low  $\text{CO}_2$  emission and energy consumption [16]. Traditional solar evaporation approaches generally have low photothermal conversion efficiencies of 30–45% arising from poor solar absorption and high heat losses, which make them an impractical approach to generate large quantities of clean water [15,17,18]. Thus, there is a need for more effective light-absorbing materials, new device designs, and modules for highly efficient SSG devices. Recently, novel light-absorbing nanomaterials have attracted immense attention. Some nanomaterials exhibit solar-to-thermal conversion efficiencies close to 100%, thus as a result, maximizing the solar water evaporation performance [15,19–22]. To date, solar absorbing materials reported as promising solar absorbers for SSG include carbon-based materials, metallic-based materials, semiconductor-based materials, and polymer-based materials. Carbon-based materials such as graphene (Gr) and carbon nanotubes (CNTs) exhibit excellent light absorption, leading to enhanced photothermal conversion efficiency [23]. However, their high cost of production limits their practical applications [24]. In addition, the hydrophobic nature of CNTs and Gr inhibit continuous contact with bulk water for evaporation [25–28]. On the other hand, hydrophilic graphene oxide experiences swelling in aqueous water [29]. Plasmonic metals exhibit excellent photothermal conversion efficiencies, yet often they are made of noble metals, which require complicated synthesis that lead to high cost for implementation at large scale [23]. Conjugated polymeric materials also exhibit good photothermal conversion efficiencies but have drawbacks in their long-term stability and recyclability.

One of the most promising photothermal materials (PTMs) is semiconductor-based material, which exhibits high photothermal conversion efficiencies, good chemical stability, is naturally abundant, and is widely adopted in many industries [24]. For instance, many

semiconductor materials (e.g., metal oxides and sulfides) exist naturally in the form of ore minerals such as pyrite ( $\text{FeS}_2$ ), chalcocite ( $\text{Cu}_2\text{S}$ ), chalcopyrite ( $\text{CuFeS}_2$ ),  $\text{MoS}_2$ , ilmenite ( $\text{FeTiO}_3$ ), and rutile or anatase ( $\text{TiO}_2$ ), which require minimal processing when used for SSG [30]. In addition, semiconductor PTMs possess antibacterial properties, long term stability, and good recyclability [31]. In semiconductor PTMs, the absorption of incoming photons induces electron-hole pairs, which then recombine to generate heat that enables steam generation and clean water production [32]. The bandgaps in semiconducting PTMs can also be tuned to capture a broad solar spectrum containing ultraviolet-visible-infrared regions, another significant advantage of semiconductor PTMs.

A search in literature revealed some recent review articles reporting on solar steam generation and its applications [19,33–37], including reviews of plasmonic metals [38] and graphene oxide [39]. However, to the authors' knowledge, no comprehensive reviews have yet been reported specifically for semiconductor-based PTMs for SSG application. Therefore, in this review, we present a thorough discussion of the preparation and SSG application of semiconductor PTMs, including the factors affecting the light-to-heat and heat-to-vapor generation, and the various proposed strategies to enhance their SSG performance for desalination and wastewater treatment. The stability performance, reusability, and recyclability of semiconductor PTMs are also discussed in this review (see Fig. 1 for various applications of SSG).

## 2. Solar steam generation configurations

SSG systems are classified into three configurations depending on the location of the PTMs (see Fig. 2): (i) PTM layer fixed at the bottom, (ii) volumetric systems where PTMs are dispersed, and (iii) interfacial systems where PTMs float on the water surface [19]. The first two systems (PTMs fixed at the bottom and volumetric systems) display low photothermal conversion efficiency due to the slow heat accumulation process where large quantities of water need to be heated before efficient evaporation can take place [19]. For systems where the PTM layer is at the bottom (Fig. 2a), solar light must travel through the bulk water before reaching the bottom solar absorber. As a result, the intensity of sunlight is reduced as it reaches the bottom solar absorber, while at the same time, this creates difficulties in raising the water temperature and evaporation to occur. [43] In the dispersed configuration case, controlling the optimum amount of PTM particles to be dispersed inside the water is critical as non-optimum amounts will either lead to insufficient and slow heat generation or reduced photothermal efficiency due to PTM shading (Fig. 2b). For the “fixed at the bottom” and volumetric systems, the evaporation efficiency is usually low which is attributed to three factors: (i) reduced solar absorption corresponding to reduced intensities and scattering of the light within the water, (ii) substantial thermal energy loss, and (iii) heat loss to the bulk water that is not involved in steam generation due to thermal diffusion [33,44].

On the other hand, a newer configuration based on floating the PTM layer on top of the water surface (interfacial design, Fig. 2c) was found to provide photothermal conversion efficiencies close to 100% [45–48]. The lower thermal conductivity of air compared to water significantly reduces heat dissipation [49]. In the interfacial system, light absorbed by the PTM is converted into heat, which induces localized heating of water at the water-air interface to enable evaporation. Heat losses can be further reduced by placing the porous thermal insulators at the bottom of the absorber. Such methods maximize the vapor generation rate and enhance the supply of water to the heated region [4,10]. Therefore, floating SSG configuration (interfacial system) is the most promising configuration in terms of photothermal conversion efficiencies and water production rates.

The efficiency in the interfacial system can be quantified using the following equation [50]:

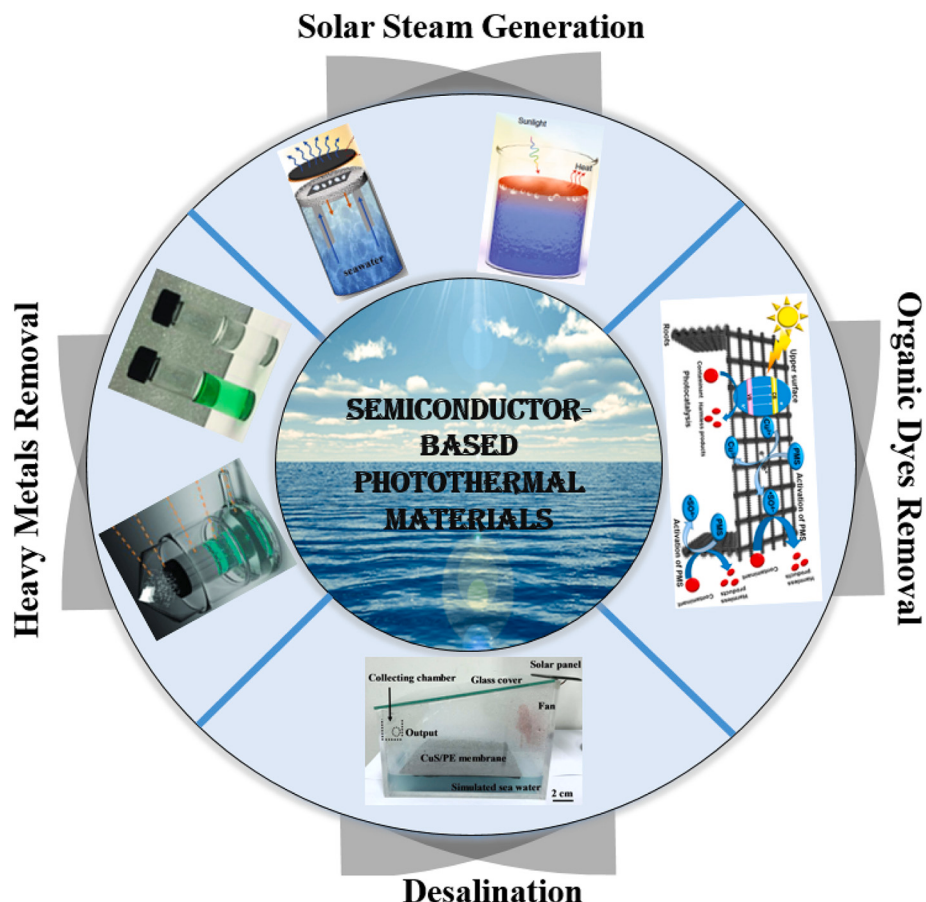


Fig. 1. Schematic of the various applications of semiconductor-based photothermal materials for solar steam generation (inset images are from [10,25,40–42]).

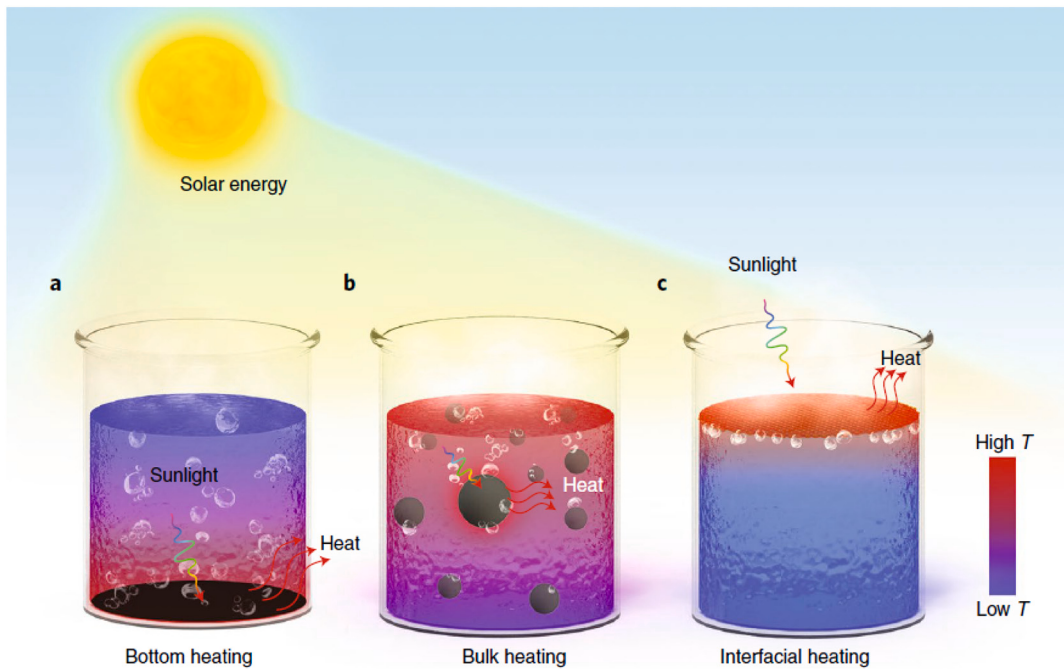


Fig. 2. Solar-driven evaporation system configurations: (a) bottom heating, (b) volumetric heating (dispersed case), and (c) interfacial heating [10].

$$\text{Solar - to - vapor conversion efficiency } (\eta) : \frac{v (C_p \times \Delta T + \Delta_{\text{vap}} H_m)}{C_{\text{opt}} I}$$

where  $v$  is water evaporation rate,  $C_p$  is the specific heat capacity of water ( $4.18 \text{ J g}^{-1} \text{ K}^{-1}$ ),  $\Delta T$  is the difference between the vapor temperature and the ambient temperature,  $I$  is the nominal direct solar

illumination ( $\sim 1 \text{ kW/m}^2$ ),  $c_{opt}$  is the optical concentration, and  $\Delta_{vap}H_m$  is the latent enthalpy of vaporization for water at the respective temperature. Mostly,  $\Delta_{vap}H_m$  at the boiling temperature of  $100^\circ\text{C}$  (i.e.,  $2257 \text{ kJ kg}^{-1}$ ) is used in the calculation. For most lab-scale experiments, one sun illumination is usually used, which has an equivalent energy density of  $\sim 1000 \text{ Wm}^{-2}$  of light irradiance.

### 3. Design and preparation of semiconductor-based PTMs for solar steam generation

#### 3.1. Engineering of light absorption

Solar irradiance at the earth's surface on a sunny day is approximately  $1 \text{ kW m}^{-2}$  (equivalent to one Sun) at sea level [51]. The solar spectrum consists of  $\sim 7\%$  ultraviolet (UV) light (300–400 nm),  $\sim 43\%$  visible (vis) light (400–700 nm), and  $\sim 50\%$  near-infrared (NIR) light (700–2500 nm) [52,53]. The optimal semiconductor PTMs for SSG should be able to capture all the wavelengths of the incident sunlight (UV-Vis-NIR) with minimum reflection and transmittance and efficiently convert the light energy to heat. This will result in achieving excellent light-to-heat conversion (photothermal conversion) efficiency [54].

Semiconducting materials excited by photons with energies greater than or equal to their bandgap generate electron-hole pairs. As excited electrons relax, energy can be released in the form of heat or vibrations by energy transfer to the material lattice (i.e., non-radiative relaxation via phonons). When the phonons encounter defects in the lattice of the material with poor thermal conductivity, heat dissipates into the surroundings, which establishes a temperature distribution depending on the optical absorption and their recombination characteristics [19,33]. Semiconductor PTMs with narrow bandgap ( $E_g$ ) can achieve excellent photothermal conversion efficiencies as most of the solar spectrum can be utilized for heat generation. Large bandgap PTMs exhibit limited optical absorption, which results in low photothermal conversion efficiencies. Besides regulating the bandgaps, nano/microstructure semiconductor PTMs contribute to excellent light absorption through sunlight reflection and trapping. Various strategies have been exploited to narrow the bandgap for enhancing the light absorption of semiconductor PTMs. See Table 1 for a summary of the strategies used to enhance the SSG performance of various semiconductor-based PTMs.

##### 3.1.1. Utilizing plasmonic semiconductor materials

Plasmonic materials with localized surface plasmon resonance

(LSPR) are capable of absorbing broad light spectrum up to the NIR region, which is beneficial for remarkable light harvesting within a wide range of the solar spectrum. The increase in the valence band leads to a plasmonic resonance peak shift to higher frequencies [55]. The LSPR can be obtained and tuned by two main methods: (i) formation of free carriers (holes) through cation vacancies due to the presence of a defect or doping [55,56] and; (ii) use of low bandgap materials to boost the absorption to cover the whole solar spectrum. The structure compositions and morphology could also play a vital role in improving light absorption [57]. Traditional noble metals have been widely used to generate the LSPR effect. However, high cost limits their practical applications, especially in solar steam generation. Interestingly, LSPR semiconductor materials with low bandgap open a new avenue as alternative candidates to noble metals. This is attributed to their relatively lower cost (precursor cost as well as fabrication cost) and potential to be synthesized at large-scale.

**3.1.1.1. Metal chalcogenides.** Non-stoichiometric p-type semiconductor  $\text{Cu}_{2-x}\text{S}$  is a well-known plasmonic semiconductor PTM in solar steam generation. It can exhibit different bandgaps through varying the crystal structures via controlling the stoichiometric ( $x$ ) in  $\text{Cu}_{2-x}\text{S}$  [55]. The stoichiometric and morphologies can be varied by controlling the synthesis parameters or precursors types. This has a significant influence on photothermal conversion efficiency [58]. For instance, Zhang et al. fabricated high-quality  $\text{Cu}_7\text{S}_4$  nanocrystals (NCs) with different shapes via heat controlled reactions with sulfur in 1-cotadecene for SSG [58]. At one sun irradiation, water evaporation efficiencies of 60.5%, 51.6%, 53.1%, and 47.8% were achieved for monodisperse disk-like, monodisperse spherical, polydisperse disk-like, and polydisperse spherical  $\text{Cu}_7\text{S}_4$  NCs, respectively. The highest performance was achieved by monodisperse disk-shaped NCs as they possess the strongest LSPR effect and have high electron (hole) carriers.

Quaternary p-type  $\text{Cu}_2\text{ZnSnX}_4$  ( $X = \text{S}$  or  $\text{Se}$ ) has received considerable attention as an effective solar absorber due to its low and tuneable bandgap [59]. For example,  $\text{Cu}_2\text{ZnSnS}_4$  was investigated as an efficient solar absorber due to its narrow direct energy bandgap and a very high optical absorption coefficient ( $> 10^4 \text{ cm}^{-1}$ ) [60,61]. Mu et al. synthesized 3D  $\text{Cu}_2\text{ZnSnS}_4$  nanosheet as an efficient solar absorber for SSG applications [62]. The strong surface plasmon resonance caused by high carrier concentration results in low bandgap and the incident light trapped between the microstructure leads to excellent light absorption properties of 92.25% at the entire solar spectrum. This results in a remarkable solar water evaporation rate and efficiency of  $1.46 \text{ kg}^{-1}$

**Table 1**

Strategies for improving the solar steam generation performance of semiconductor-based PTMs based on the design feature, their limitations, and modifying approaches.

Feature	Methods	Limitation	Modifying approach
Light absorption	<ul style="list-style-type: none"> <li>Narrow the bandgap.</li> <li>Regulate the structure composition of the materials.</li> </ul>	<ul style="list-style-type: none"> <li>Some of the approaches to narrow and enhance the optical properties are complicated.</li> </ul>	<ul style="list-style-type: none"> <li>Morphology constructions.</li> <li>Design nanocomposite materials.</li> <li>Synthesize porous materials.</li> </ul>
Water supply	<ul style="list-style-type: none"> <li>Water supply through the structure of the material.</li> <li>Use of hydrophilic substrate with external water supply.</li> </ul>	<ul style="list-style-type: none"> <li>Control the concentrations and morphologies for a fast escape of water vapor.</li> </ul>	<ul style="list-style-type: none"> <li>Regulate the concentrations of the semiconductor PTMs materials.</li> <li>Control parameters of PTMs (Porosity, thickness, and dimensions).</li> </ul>
Thermal management	<ul style="list-style-type: none"> <li>Integrating semiconductor PTMs with a low thermal conductive substrate and adding external insulator.</li> <li>Designing 3D devices</li> </ul>	<ul style="list-style-type: none"> <li>Convection and radiation heat losses in the 2D SSG devices (planar design).</li> </ul>	<ul style="list-style-type: none"> <li>Control the substrate compositions and properties.</li> <li>More research focuses on 3D SSG devices.</li> <li>Microstructure semiconductor materials could localize the heat within the structure compositions.</li> </ul>
Anti-salt crystallization	<ul style="list-style-type: none"> <li>Synthesizing hydrophobic semiconductor materials.</li> <li>Coating hydrophilic materials with a hydrophobic layer.</li> </ul>	<ul style="list-style-type: none"> <li>Hydrophobic materials might lower the water evaporation rate.</li> <li>Coating with a hydrophobic layer (silane) for nanosize materials might not be stable for long-term and is cost adding.</li> </ul>	<ul style="list-style-type: none"> <li>Combination with microporous hydrophilic substrates.</li> <li>Design hydrophilic and anti-salt materials that resist salt accumulation.</li> <li>Conduct a computational calculation approach.</li> </ul>

$\text{m}^{-2} \text{ h}$  and 84.5%, respectively, under 1 sun irradiation.

Similar to the quaternary sulfide, selenide p-type  $\text{Cu}_2\text{ZnSnSe}_4$  (CZTSe) with narrow bandgap ( $E_g = 0.88$  to  $1.2$  eV) has been demonstrated as potential solar absorber [63]. This quaternary p-type displays excellent light absorption, and more research on this direction can be considered. For example, Yang et al. demonstrated CZTSe nanocarambolas and irregular shapes for highly efficient SSG [64]. The optical properties of quaternary p-type display strong LSPR that covers the full solar spectrum. The high free carrier (hole) density of the nanocarambolas and the unique assembled nanoporous structure hence achieve a strong LSPR effect in the IR region. This results in excellent photothermal conversion in the absorber layer to evaporate the water at the interface and exhibit a high water evaporation rate of  $1.52 \text{ kg m}^{-2} \text{ h}^{-1}$ , at one sun illumination. On the other hand, the irregular shape displayed a weak LSPR effect, resulting to a low water evaporation rate of  $1.412 \text{ kg m}^{-2} \text{ h}^{-1}$ . However, despite the exceptional performance, the high toxicity of selenium added during the synthesis process remains a challenge that could hinder the applications of these materials for SSG application.

Previous works revealed that metal chalcogenides possess excellent light absorption characteristics. Most especially, copper sulfides feature merits of low-cost, easy synthesis process. They can be formed in various morphologies and sizes, making it easy to be integrated with several types of substrates for enhancing the optical properties. So far, this unique class is the most promising semiconductor PTMs due to its excellent solar water evaporation performances. On the other hand, in the case of binary metal chalcogenides, despite the excellent display performance, more investigations are required regarding the structure compositions and morphology regulations.

**3.1.1.2. Oxygen deficient metal oxides.** Transition metal oxides (TMOs), such as tungsten oxide ( $\text{WO}_3$ ) or molybdenum oxide ( $\text{MoO}_3$ ), have attracted considerable attention as excellent PTMs mainly attributed to their excellent thermal stability [65–67] and their unique characteristics of the free outer-d valence electrons. Their bandgap can be regulated through phase transitions, as the occupancy level of its 5d orbitals varies with lattice distortion [68]. Oxygen-deficient metal oxides possess high charge carrier density, which is necessary for achieving the LSPR effect. This also acts as a defect for phonon propagation, leading to expected enhancement in photothermal conversion efficiency in SSG application. Additionally, introducing oxygen vacancy results in the appearance of defect energy levels and reducing the gap between the valence band and the defect level [69,70].

Tungsten oxide,  $\text{WO}_{3-\text{x}}$  (e.g.,  $\text{WO}_{2.72}$ ,  $\text{WO}_{2.83}$   $\text{WO}$ , and  $\text{W}_{19}\text{O}_{49}$ ) with oxygen defects is an attractive LSPR candidate for SSG. Amorphous  $\text{WO}_3$  possesses large lattice distortion and displays a wide bandgap of  $E_g = 3.4$  eV; while the monoclinic crystalline phase exhibits  $E_g = 2.6$  eV [68,71]. After introducing the oxygen vacancy, nonstoichiometric  $\text{WO}_{3-\text{x}}$  displays strong broad light absorption in the NIR region due to inter-valence charge transfers, LSPR of free electrons, small polariton absorption and narrower bandgap [32]. Sun et al. reported the phase transition from semiconductor metallic  $\text{WO}_3$  to quasi-metallic through a hydrogenation process, delivering excellent light absorption characteristics of 90.6% [72]. Furthermore, ab initio calculation showed a narrower bandgap of  $\text{WO}_{2.9}$  compared to  $\text{WO}_3$ , consequently extending the range of light absorption wavelengths from UV to Vis to NIR region.

Additionally, the band structure of  $\text{WO}_{2.9}$  shows that both the top of the valence band and bottom of the conduction band is partially occupied, with its Fermi energy level shifted nearer to the conduction band. Fang et al. designed and fabricated a flexible, self-floating  $\text{W}_{18}\text{O}_{49}$  nanowires/carbon foam composite through a hydrothermal and annealing process using melamine foam as a raw precursor for carbon-based support [73]. During the annealing process, the melamine foam was converted into carbon foam with a highly porous net structure, which contributed to the scattering and trapping of the light. In

addition, the total amount of reduced  $\text{W}_{18}\text{O}_{49}$  ( $\text{W}^{5+}$  or  $\text{W}^{4+}$ ) was increased from 16.7% to 45%. This results in intensive oxygen vacancy and enhances the light absorption characteristics. For this reason, a high water evaporation rate of  $1.694 \text{ kg m}^{-2} \text{ h}^{-1}$  was obtained under one sun illumination. The flexible features of the composite make it reusable for several cycles with stable performance. Chang et al. demonstrated a flexible solar steam generator composed of nonstoichiometric  $\text{W}_{18}\text{O}_{49}$  mesocrystals wrapped with PDMS on PTFE membranes [74]. The mesocrystals materials consist of high oxygen vacancies, leading to strong LSPR, and broadband light absorption with a bandgap of 2.7 eV. This bilayer exhibited a water evaporation rate of  $1.15 \text{ kg m}^{-2} \text{ h}^{-1}$ , and efficiency of 80.7% under one sun irradiation.

$\text{MoO}_x$  is another example of oxygen-deficient metal oxides with strong LSPR properties, making it promising PTMs for SSG applications. For example, Lu et al. employed an oxygen-deficient  $\text{MoO}_x$  flower-like structure composed of atomically thick nanosheets [75]. The light absorption of ~90% was obtained, corresponding to a bandgap of 1.82 eV. The material was loaded onto the PTFE membrane and applied as a solar steam generator where a water evaporation rate of  $1.255 \text{ kg m}^{-2} \text{ h}^{-1}$  and an efficiency of 85.6% were achieved. Guo's group presented the work on using  $\text{MoO}_{3-\text{x}}$  quantum dots as PTM, where its absorption band closely matched with the solar spectrum [69]. The oxygen vacancy was introduced by the hydrothermal method utilizing chitosan as both reducing and capping agent. After loading the materials into cellulose acetate membrane and coated with fluoroalkylsilane, a water evaporation rate of  $4.95 \text{ kg m}^{-2} \text{ h}^{-1}$  and an efficiency of 62% were demonstrated under 5 sun illumination.

Oxygen deficient metal oxides are good materials with a lower bandgap and strong LSPR effect for achieving excellent light absorption for solar water evaporation. To further upgrade the water evaporation performance, more research needs to be conducted regarding tailoring morphology control (e.g., porous, size and diameter) or through nano-composite design.

### 3.1.2. Two-dimensional (2D) layered materials

Layered 2D materials have recently been reported as promising materials in SSG, due to their excellent-photothermal conversion efficiency. The materials exist or are formed in the planar surface with poor solar absorbance due to the high light reflection. Therefore, it is crucial to modify the surface and the structure for enhancing the optical properties and water evaporation performance.

Molybdenum disulfide ( $\text{MoS}_2$ ) is an exciting semiconductor material consisting of three chemically bonded atomic layers, S-Mo-S, which are stacked by van der Waals forces.  $\text{MoS}_2$  is classified based on stacking layers: one layered-stacked as trigonal (1T- $\text{MoS}_2$ ), two-layered stack hexagonal polymorph (2H- $\text{MoS}_2$ ), and three-layered-stacked rhombohedral (3R- $\text{MoS}_2$ ) [76–78]. The materials have several advantages, such as they exist naturally and have lower toxicity than other carbon-based 2D materials [25,79–81]. The pores and defects in  $\text{MoS}_2$  nanosheets were expected to be highly ion-selective and water permeable [25]. These fascinating features make  $\text{MoS}_2$  a promising PTM for SSG. For example, the phase change from 2H to 1T after the lithiation exfoliation process consequently narrows the bandgap and results to excellent solar-light absorption characteristics [82]. After loading on to BNC hydrogel, the bilayer structure revealed water evaporation efficiency of 76%, and 81% under 0.76 sun and 5.35 sun irradiation, respectively [82]. However, synthesizing a stable 1T phase remains a challenge as it is easily transformed back to the 2H phase. In a most recent study, Hu's team proposed a novel 3D dimpled 2H- $\text{MoS}_2$  membrane with a microporous structure (1–2  $\mu\text{m}$ ) for highly efficient SSG desalination (see Fig. 3b for the SEM images) [25]. This unique structure was fabricated via microwave-and thermal annealing process using a mixture of 1T and 2H phases. The solar steam device was composed of the floated dimpled 2H- $\text{MoS}_2$  membrane, PS foam under the membrane, and a fiber as water channel, as illustrated in Fig. 3a. Outstanding water evaporation efficiencies of 83 and 91% were achieved, under 1 and 3 sun irradiation,

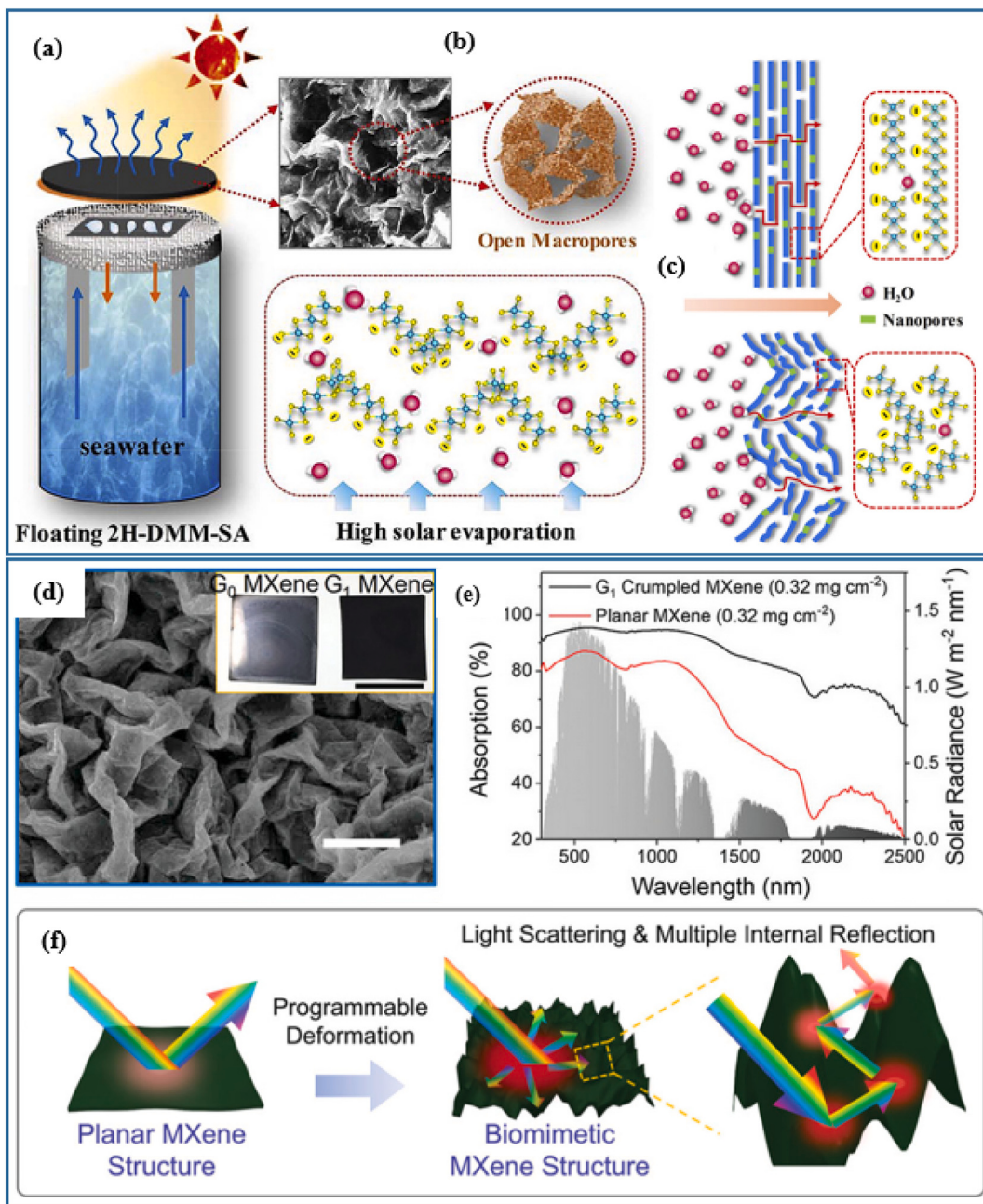


**Fig. 3.** (a) Solar steam generation device of 3D dimpled 2H-MoS<sub>2</sub>, (b) SEM image of the sharply dimpled surface with a large amount of protrusions of the 2H-MoS<sub>2</sub> membrane, (c) the proposed mechanism for high water transport rates of the MoS<sub>2</sub> membranes [25], (d) SEM image of Biomimetic MXene structures and UV-Vis-NIR spectrum broadband light absorption, (e) light absorption performance of crumpled MXene and planar MXene, and, (f) schematic illustration comparing the mechanism of light absorption in Planar MXene and biomimetic MXene nanocoating [87].

respectively. Moreover, the molecular dynamic simulations revealed that water evaporation took place via inherent nanochannels of the sharply dimpled surfaces (Fig. 3c). Other reported strategies that could be implemented in SSG applications are 2D MoS<sub>2</sub> nanosheet-based super-lattices [83], the formation of hetero-layers with other 2D materials [84], and forming an alloy of sulfur and selenium (MoX<sub>2</sub>: X = S and Se) [85]. All these strategies could be applicable in using semiconducting 2D materials in SSG applications. Finally, the fabrication of a microporous 2D structure is a promising strategy for highly efficient systems. However, more studies on porous MoS<sub>2</sub> architectures via control of surface morphology and pore-size, and interlayer distance are worthy of investigation.

MXenes are a new family of multi-functional 2D materials with the

general formula of M<sub>n+1</sub>X<sub>n</sub>T<sub>x</sub>, where M represents a transition metal. T<sub>x</sub> represents surface functional groups (e.g., OH, O, and F groups) while X represents C or N, n = 1, 2, or 3 [86]. The materials are being increasingly investigated as a remarkable shielding PTM for SSG applications. This is attributed to their high light-to-heat conversion efficiency, which could even reach 100% [22]. However, the planar surface of MXene can have high light reflections, leading to low solar-to-thermal conversion efficiency. To address this challenge, providing microporous structure on MXene has been proposed as an efficient strategy to promote light absorption by extending the optical path for multiple scattering. For instance, Zhao et al. transformed 2D MXene to 3D architectures by assembling MXene nanosheets (3.4 mg cm<sup>-3</sup>) onto the melamine foam (MF) using polyvinylalcohol (PVA) as an adhesive agent. The

outstanding light absorption of ~95% at a range between 350 and 1500 nm was achieved, which is sufficient to generate sufficient photothermal conversion efficiency of 88.7% under one sun irradiation. Yet, the high concentrations of MXene resulted in an expensive process and limited its manufacturing and practical applications. Li et al. designed and fabricated a biomimetic 2D crumpled MXene for highly efficient SSG (Fig. 3d) [87]. 2D crumpled MXene with a low concentration (0.32 mg cm<sup>-2</sup>) was spray-coated on thermally responsive polystyrene (PS) substrates. After being air-dried, the planar MXene was heated above the glass transition temperature of PS (100 °C) at which point the MXene shrunk to 50% of the original length and 25% of the area. This resulted in the deformation into an isotropic crumpled nanostructure. They found that after the first deformation of planar MXene nanocoating was deformed into isotropic crumpled structures, the incident light was strongly scattered and reflected multiple times causing broadband light absorption of 84.9–86.9% UV–Vis–NIR. After the second and third deformations, the light absorption was further improved up to 93.2% (Fig. 3e). The schematic illustration describing this phenomenon is shown in Fig. 3f. The SSG performance was conducted under one sun illumination, and a water evaporation rate of 1.33 kg m<sup>-2</sup> h<sup>-1</sup> was achieved.

In summary, one of the promising approaches to achieve excellent light absorption and light-to-heat conversion is through designing porous microstructures in MXene. The light-to-heat conversion approach is not enough to achieve a remarkable water evaporation rate/efficiency. To improve such a measure, the structure design of this material should be further enhanced. It will be interesting to investigate the role of integrating various substrates with MXene or nanocomposite for improving the overall water evaporation efficiency. Besides, a primary obstacle preventing the applications of this material is the complicated fabrication process and cost.

### 3.1.3. Metal-doped semiconductors

Doping large bandgap semiconductor materials with plasmonic nanoparticles (NPs) has been proposed as a promising approach for enhancing the photothermal conversion efficiency through narrowing the bandgap [88–90]. Plasmonic metals NPs display a heating effect and can effectively lower the bandgap in semiconductor materials [91]. For instance, plasmonic Ni NPs were used to cover TiO<sub>2</sub> nanotubes resulting in optical absorption of 97% across the full solar spectrum [92]. Bilayer Au-TiO<sub>2</sub> core-shell NPs comprising different crystal shells with a thickness of ~100 nm were synthesized as an efficient PTM for SSG applications [91]. The absorption peak of Au NPs was red-shifted from 527 nm to 603 nm, compared to the hollow TiO<sub>2</sub> NPs, which only red-shifted from 330 nm to 345 nm. Water evaporation rate as high as 0.86 kg m<sup>-2</sup> h<sup>-1</sup> with an efficiency of 53.6% was achieved upon one-sun irradiation. Apart from that, researchers have tried to improve the photothermal conversion and water evaporation efficiency using a low-cost plasmonic metal such as Al. For instance, Yi et al. developed an inexpensive and highly scalable synthesis strategy to obtain black TiO<sub>x</sub> using plasmonic Al [93]. They synthesized the material via fabricating TiO<sub>2</sub> NPs with metallic Al with the assistance of molten AlCl<sub>3</sub> in an inert atmosphere. After incorporation with poly(-vinylidene fluoride) (PVDF) via a phase inversion method, a self-floating mesoporous photothermal composite was obtained. The plasmonic effect, mesoporous structure and black-body effect lead to excellent light absorption of 90.2% (UV–Vis–NIR). At one sun illumination, a water evaporation rate of 1.17 kg m<sup>-2</sup> h<sup>-1</sup> was achieved. To further improve the metals doping, several methods are suggested: (i) it is necessary to investigate the size and distribution of plasmonic metals on the semiconductor materials; (ii) incorporating plasmonic NPs with metals chalcogenides or oxide to boost the plasmonic effect for higher solar conversion efficiency; and (iii) implementing reliable deposition or coating methods.

### 3.1.4. Size, concentrations, and other parameters

An effective approach to adjust bandgap is to tailor the material size

with a narrow size distribution. As an example, titanium dioxide (TiO<sub>2</sub>) exists in different crystal phases (i.e., anatase, rutile, brookite) and exhibits wide  $E_g$  (3–3.2 eV). As a result, the optical absorption is limited to the UV region (<400 nm), accounting for a total of <7% of the solar spectrum [89,94]. Wang et al. reported nanoscale titanium sesquioxide (Ti<sub>2</sub>O<sub>3</sub>) NPs (size ~400 nm) using a ball milling process and obtained a very small bandgap of 0.1 eV. The corresponding bandgap mechanism is illustrated in Fig. 4a [95]. The light absorption characteristics are compared to the commercial bulk Ti<sub>2</sub>O<sub>3</sub>. The bulk one shows less light absorption capability (85.4%) compared to nanosize Ti<sub>2</sub>O<sub>3</sub> NPs (92.5%), due to the less efficient light scattering of bulk particles (Fig. 4b). To investigate the effect of NP size, they reduced the size to 350 nm and this resulted in 1% increase in the light absorption. Also, the materials demonstrated a 100% conversion of the entire absorbed light into heat. After loading Ti<sub>2</sub>O<sub>3</sub> NPs on cellulose membranes, a remarkable water evaporation rate of 1.32 kg m<sup>-2</sup> h<sup>-1</sup> under one sun illumination was obtained. Besides the size, the concentration of semiconductor PTMs displays a vital role in enhancing the optical characteristics. For example, Tao et al. investigated the impact of the plasmonic CuS concentrations in light absorption [96]. They incorporated different amounts of CuS (1 to 12 mg) into the PVDF membrane. The light absorption was increased with increasing the amounts of CuS concentrations reaching to a maximum (12 mg) absorption of >90% in the UV–vis and >96% in the NIR region (Fig. 4c). With excess amounts of CuS (16 mg), they found no difference to the optimum loading case (12 mg) as it reaches the saturation level. 12 mg-CuS-PVDF leads to a water evaporation rate of 1.43 kg m<sup>-2</sup> h<sup>-1</sup>, 2.91 kg m<sup>-2</sup> h<sup>-1</sup>, and 5.93 kg m<sup>-2</sup> h<sup>-1</sup> under 1 sun, 2 sun, and 4 sun illumination, respectively (Fig. 4d). In contrast, Chen et al. presented a MoS<sub>2</sub> nanoflower structure with an external diameter of 1 μm composed of nanosheets deposited on air-laid paper (ALP) as efficient PTMs. They realized that by changing the concentration of MoS<sub>2</sub> into the ALP layer, the light absorption efficiency also varies until no change is observed [97]. Yang et al. reported the hybrid composite material of MoS<sub>2</sub> nanosheets with single-walled CNTs by controlling the thickness of nanosheets from 2 to 6 nm, the solar absorption was enhanced from 82% to 95% [98]. The surface roughness causes the multi-scattering and trapping of incident solar irradiation that enhances light absorption [99]. CuS/PE composite membrane was also prepared to feature rough 3D surface and open porous channels, leading to light absorption of ~93%, low transmittance of ~2.5%, and reflectance of ~4% [42]. The growing semiconducting PTM on a rough membrane or 3D supports, such as metal foams, would be a desirable SSG application approach. Regulating the thickness and concentrations of semiconductor PTMs not only impact on the light absorption but also the water evaporation efficiency. Future studies should explore the relationships and the effects of the PTM thicknesses and concentrations on light absorptions and water evaporation rate.

## 3.2. Designing semiconductor solar water evaporation devices

### 3.2.1. Thermal management through the substrate and structural design

Thermal management is critical for the effective performance of an interfacial SSG system. In an ideal case, all generated heat is utilized to evaporate the water, but due to interfacial SSG configuration, heat losses are unavoidable. Heat is lost by conductive and radiative processes from the solar absorber to the water beneath it and by convective and radiative processes to the surroundings (Fig. 5b) [4,23]. For example, the conventional design of a hydrophobic solar absorber attached on top of a hydrophilic porous floating support exhibits inherent thermal loss issues. The adjacent water can fill the gaps in the hydrophilic support layer, replacing air voids and increasing conductive thermal losses as water has higher thermal conductivity than air [100]. Improvements to the interfacial SSG systems design include 2D and 3D solar water evaporator configurations (Fig. 5a). The energy losses in solar water evaporation, including conduction, radiation, and convection, can be calculated by the following equations [20,23,101]:

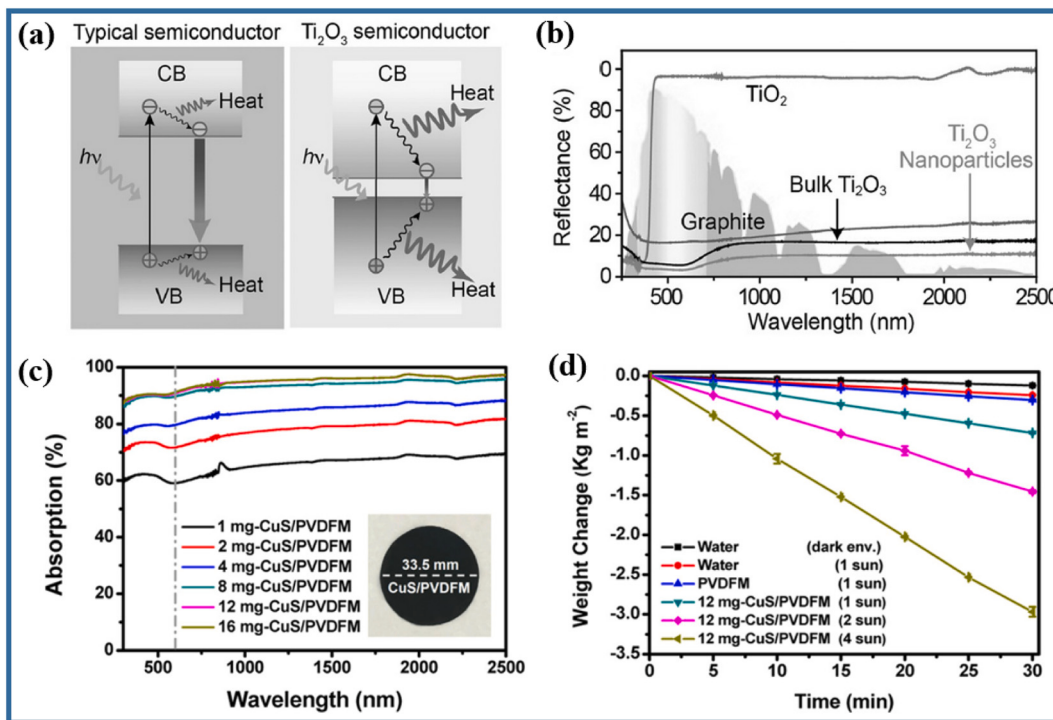


**Fig. 4.** (a) Illustration of electron-hole generation and relaxation in a typical semiconductor (left) and narrow bandgap Ti<sub>2</sub>O<sub>3</sub> (right), (b) solar reflectance spectra of Ti<sub>2</sub>O<sub>3</sub> NPs [95], (c) UV-vis-NIR absorption spectra of different amount CuS/PVDFMs, and (d) water evaporation rate of 12 mg-CuS/PVDFM under increasing solar intensities irradiation [96].

#### Conduction:

Conduction loss P<sub>cond</sub> is based on Fourier's law.

$$P_{\text{cond}} = Cm\Delta T \quad (1)$$

where C is the specific heat capacity of water (4.2 J °C<sup>-1</sup> g<sup>-1</sup>), m is the weight of bulk water and ΔT is the temperature increase of the bulk water after stable steam generation;

#### Radiation:

$$P_{\text{rad}} = \epsilon A \sigma (T_1^4 - T_2^4) \quad (2)$$

where P<sub>rad</sub> is radiation heat flux, ε is the emissive rate, A is the surface area, σ is the Stefan-Boltzmann constant, T<sub>1</sub> is the average temperature of the absorber, and T<sub>2</sub> is the ambient temperature;

#### Convection:

The convection loss P<sub>conv</sub> can be calculated by Newton's law of cooling.

$$P_{\text{conv}} = h(T_1 - T_2) \quad (3)$$

where P<sub>conv</sub> is convection heat flux, h is the convection heat transfer coefficient (assumed to be 10 W m<sup>-2</sup> K<sup>-1</sup>).

**3.2.1.1. 2D solar steam generation system.** Earlier studies on 2D interfacial SSG systems were based on thin hydrophobic layers of solar absorber directly floating on the water. There were high thermal losses due to direct contact with water. To minimize the heat losses, a supporting layer to act as both a thermal insulator and floating material is usually added [100]. This also isolates the solar absorber from the bulk water forming a common interfacial 2D SSG design. This strategy has attracted increased interest from many research groups as such design improved the water evaporation rate. Polymeric materials are usually used for this insulating support layer. For example, Ques's group demonstrated the use of MXene membrane with external polystyrene foam as a thermal insulator [102]. Their design enabled heat

localization with less conduction heat loss leading to a more stable temperature on the evaporation surface (~ 39 °C). Some researchers have opted to modify the supporting substrate to mitigate the heat loss drawback. For example, metal foam substrates have also been utilized as they possess high porosity and low thermal conductivity.

Xu et al. fabricated CuO nanowires on a copper foam with low thermal conductivity of 0.02 W m<sup>-1</sup> K<sup>-1</sup> using a solution-based flame treatment method [40]. For SSG application, they designed a device consisting of external expandable polyethylene EPE foam with low thermal conductivity underneath the CuO layer; consequently, the heat losses considerably reduced. Upon solar illumination under one sun, the light was converted into heat by the CuO nanowires with a temperature of 32.5 °C. Furthermore, they observed a negligible increase in bulk water temperature (~1 °C) after 30 min of light illumination under one sun. This displayed insignificant heat conduction from the solar evaporation surface to the bulk water. As a result, a water evaporation rate of 1.45 kg m<sup>-2</sup> h<sup>-1</sup> with an efficiency of 84.4% was achieved. A substrate with 3D interconnected microstructure such as natural wood, hydrogel, and PU sponge substrates display low thermal conductivity and excellent heat localization. Besides, air with low thermal conductivity passes along with the vapor and provides additional thermal insulation. These distinctive features make it a suitable substrate for high-efficiency semiconductor PTMs devices. For example, environment-friendly natural wood possessing mesoporous structures and open microchannels have been utilized with semiconductor PTMs [65,103,104]. Liu et al. combined CuFeSe<sub>2</sub> NPs ( $E_g \sim 0.45$  eV) into the microporous channel in the wood substrate [103]. At 1 sun irradiation, the surface temperature of the black wood increased from 20.1 °C to 62 °C at the dry state and 30.1 °C at the wet state. On the other hand, the blank raised to 41.7 °C at the dry state and a negligible increase in the wet state. The solar-to-heat conversion results indicated that incident light is being effectively converted to heat. This resulted to a water evaporation efficiency of 67.7% and 85.2% under 1 and 5 suns irradiation, respectively, which is attributed to the good thermal insulation provided by the wood substrate. Recent studies in SSG concluded that combinations of PTMs with

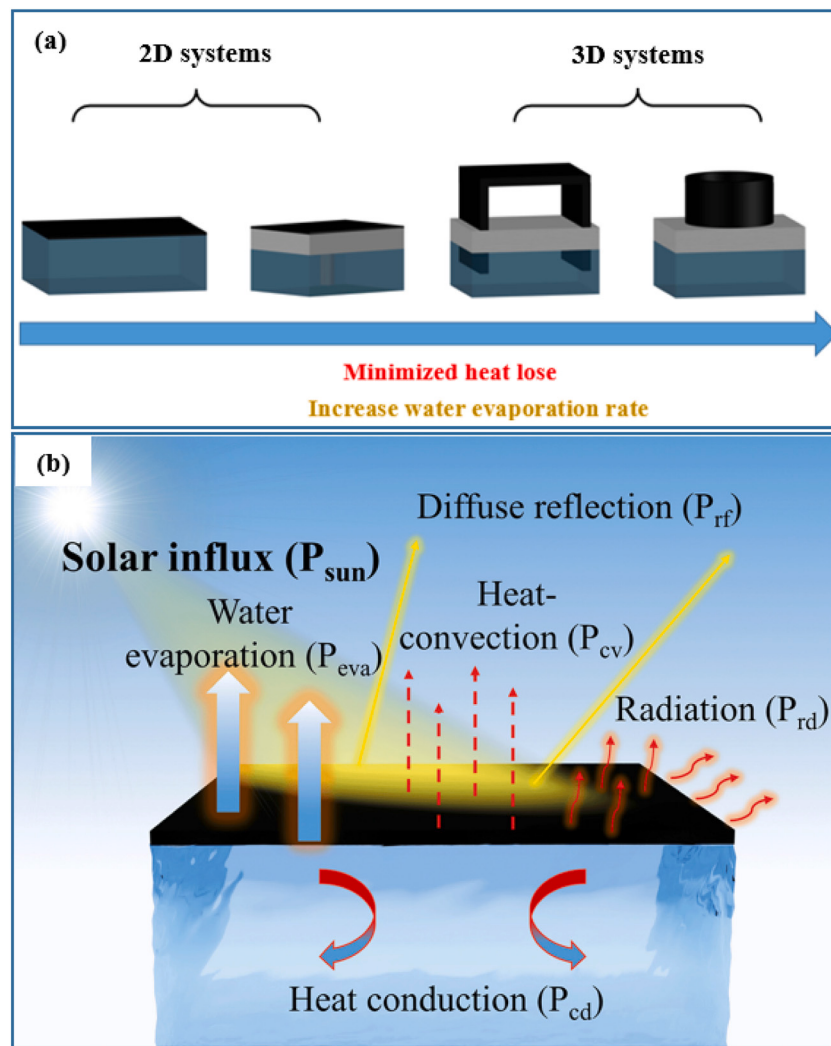


**Fig. 5.** (a) Applied interfacial solar steam generation systems and various module designs in semiconductor-based PTMs, (b) energy balance of a solar steam generation process based on air/water interfacial system [13].

low thermal conductivity 3D porous substrate are an effective approach for localizing heat and insulating properties, which will be beneficial for applications in semiconductor PTMs. Furthermore, future research directions should focus on how different substrate characteristics and the added amount of semiconductor PTMs impact the heat management of the SSG devices.

**3.2.1.2. 3D solar steam generation system.** To improve SSG device efficiencies, researchers came up with a unique design to enhance the photothermal conversion and minimize the heat losses. In recent years, 3D SSG device design has been explored for highly efficient SSG devices, which can exceed the theoretical solar evaporation limit in some reports [31,46]. The system proves to overcome the convection and radiation issues of the 2D design configuration discussed above. Furthermore, the system could recover or reabsorb the energy lost and harvest energy from the environment [50,105] or reduce the downward heat loss through the air-gap, which acts as an insulating barrier [105]. The designing of 3D solar steam generators has been rarely reported in regards to semiconductor PTMs [31,50,106]. For instance, Peng et al. developed a unique 3D cup-shaped solar absorber coated with CuFeMnO<sub>4</sub> pigment. They found that the diffuse reflectance and thermal radiation energy can be recovered, which was not observed in the 2D disk [31]. This is attributed to the 3D design, which can: (1) recover the diffuse light reflectance and thermal radiation from the cup bottom

through the cup wall, and; (2) gain energy or capture heat from the external environment through a heat exchange. As a result, remarkable water evaporation rate and efficiency of ~100% and 2.04 kg m<sup>-2</sup> h<sup>-1</sup> were achieved, respectively, under one-sun illumination. Huang et al. presented a novel approach for designing an SSG device [105]. The authors prepared dual-phase Cu<sub>2-x</sub>S on Cu foam with 3D hierarchical branch architecture with a synergistic increment of the LSPRs and the bandgap absorption (Fig. 6a). Fig. 6b reveals the proposed design bridge shape with an air-gap below the top absorber part, act as a thermal insulator barrier beside PS foam to suppress the downward heat loss. Also, the as-designed 3D system allows the energy from the environment to contribute. The two tails in serve as a water pathway channel (Fig. 6d). Under one-sun irradiation, radiation and convection heat losses of 4.4% and 1.6%, respectively, were detected by IR images visualizing the heat distribution on the top and side of the device (Fig. 6e). This caused an impressive water evaporation rate and efficiency of 1.96 kg m<sup>-2</sup> h<sup>-1</sup> and 94.5%, respectively (Fig. 6c). These fruitful findings in 3D semiconductor SSG devices revealed the critical role of the device design for achieving exceptional water evaporation rate/efficiency. Therefore, more future research should be focused on incorporating semiconductor PTMs with innovative 3D designs, which might bring the technology to the real practical applications.

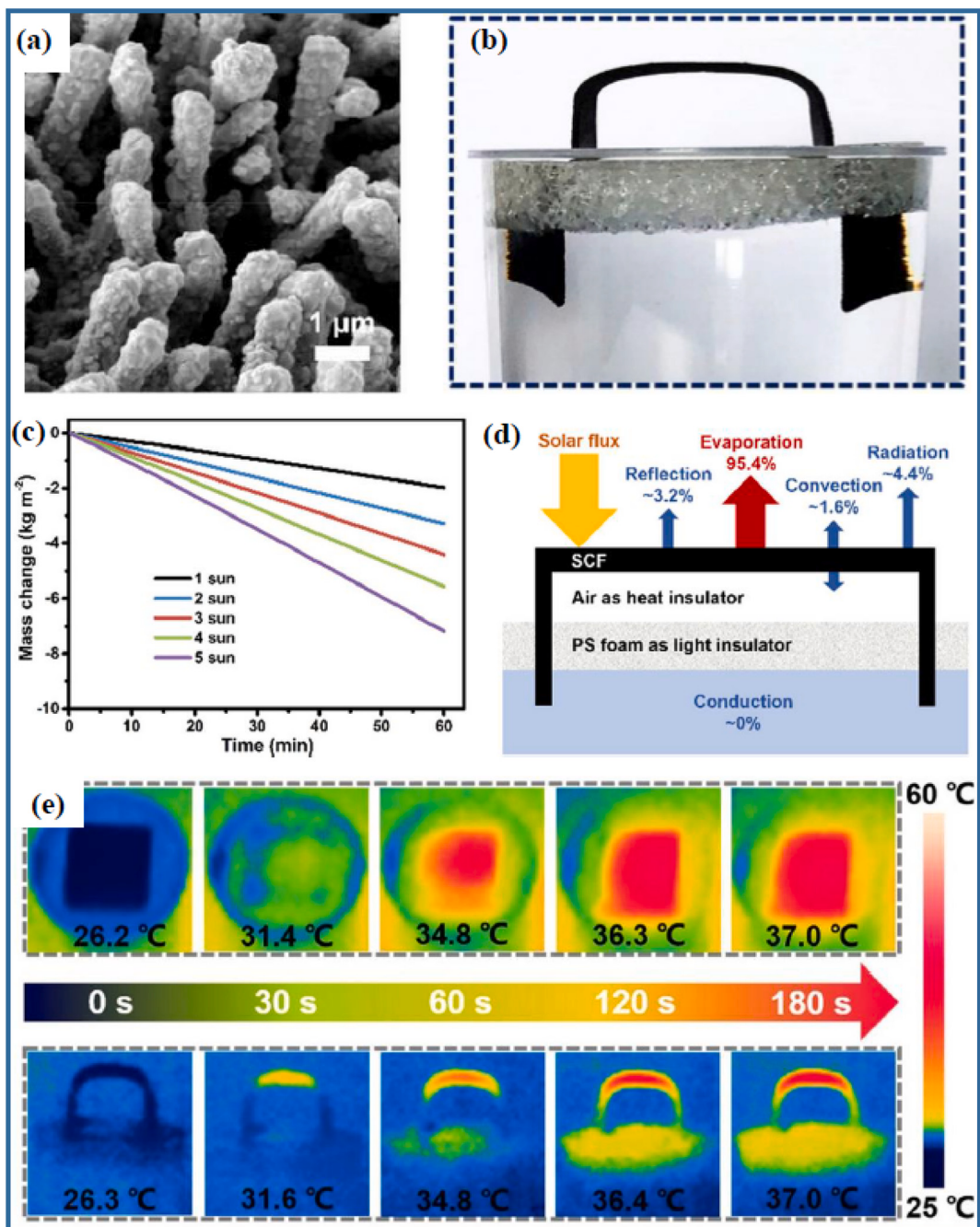


**Fig. 6.** (a) SEM images of 3D hierarchical branch architecture Cu<sub>x</sub>S/Cu foam, (b) photograph of the device fabricated with the bent Cu<sub>x</sub>S/Cu foam, (c) water evaporation under different light intensities for Cu<sub>x</sub>S/Cu foam, (d) energy balance and heat loss diagram of Cu<sub>x</sub>S/Cu foam under 1 sun illumination, and (e) IR thermal images of top-view and side-view of the water-wetted Cu<sub>x</sub>S/Cu foam under 1 sun illumination [105].

### 3.2.2. Water supply pathway

In interfacial SSG, the substrate plays a vital role in supplying water to the solar absorber part. The bottom substrate should possess a hydrophilic and porous structure for water permeation to the solar absorber part through capillary action [107]. However, low wettability restricts the heat-to-water evaporation efficiency due to insufficient water supply [108]. Various substrates such as cellulose membrane (CM) [64,69,95,102,109,110], air-laid paper [97], PVDF [93,96,111], semipermeable collodion membrane [55], and polyethylene have been used to provide both as insulating support and water pathway [42]. Wicking pathways are specially designed within or around the insulating support or as a fully isolated system from the solar absorber, directly not in contact with bulk water, while a free-air gap exists

between them.

Moreover, 1D and 2D capillary water channels are added in the system connecting the absorber part and feedwater to enable the fast wicking of water to the solar absorber. For example, Chen et al. used air-laid paper to wrap around an expandable polystyrene support layer to act as 2D water transport channel toward hydrophilic MoS<sub>2</sub> absorber. The excellent water capillary actions and wettability leads to a water evaporation rate of 1.27 kg m<sup>-2</sup> h<sup>-1</sup> [97]. On the other hand, Wu et al. employed a photothermal-water contactless system composed of CuS-agarose aerogel as PTM, insulator foam as a thermal insulator, and cotton rod as a 1D water channel to transport the water to the PTM part (evaporation area) [112]. A new approach has been suggested by using substrates with 3D interconnected microchannels such as biomass wood,

PU foams, and hydrogels structure, which have the ability to absorb a large amount of water with heat localization effects. This design also does not require additional wicking materials or thermal insulators. Sun et al. reported the efficiency of macroporous polyacrylamide hydrogel with copper sulfide as a highly efficient water transport system. The macroporous hydrogel is capable of absorbing a sufficient amount of water and allow water vapor to escape, while copper sulfide absorbs the incident light, which is trapped through the macroporous hydrogel structure, resulting in a water evaporation efficiency of 92%. Researchers also utilized biomass materials such as wood and cotton as a natural water pathway. Wood composed of cellulose, rich in hydroxyl group, prevents the detachment and agglomeration of the CuFeSe<sub>2</sub> NPs from the substrate [103]. In addition to that, the porous microchannel structure of the wood facilitates water transport to the absorber part. As a result, water evaporation efficiency of 67.7% and 85.2% was achieved under 1 and 5 suns, respectively. Other factors such as absorbers' surface porosity and roughness, concentration, and the distance from the absorber to the bulk water are significant factors affecting the water evaporation performance. For example, CuS NPs attached to polyethylene (PE) membrane with open, microporous channels of  $\sim 73.9\text{ }\mu\text{m}$  generated enough capillary forces to enable the replenishment of water to the CuS/PE membrane surface as the water evaporates from the absorber regions (Fig. 7b) [42]. Chen et al. observed that after increasing

the concentration of MoS<sub>2</sub>, the evaporation rates were also increased [97]. However, after reaching an optimum MoS<sub>2</sub> concentration, the heat exchange velocity reduced, leading to a slightly lower water evaporation rate (Fig. 7a) [113,114]. Yao et al. investigated the effect of the absorber-to-water surface distance using SnSe/NF and found that 1 mm (tested between 1, 5, and 10 mm) distance produced the highest evaporation rate [99]. Despite the excellent water transport, the design of the supporting layer is an aspect that needs further investigation to improve the efficiency of the SSG device.

### 3.2.3. Strategy to mitigate salt crystallization

Salt crystallization is one of the main issues in SSG devices for seawater desalination, as it ultimately negates its long-term stability. Hence it is considered a significant problem for its practical long-term operation [115,116]. As salted water wicks toward the absorber surface, water is evaporated, leaving excess salts to crystallize at the absorber surface. The accumulation of salts on the solar absorber blocks the exposed areas for water to wick and evaporate, leading to low evaporation rates. Moreover, less light can penetrate due to salt presence, thereby reducing the light-to-heat conversion efficiency. Therefore, it is essential to address its long-term stability issue by designing an anti-salt crystallization system. One approach is by making the solar absorber surface hydrophobic. In this way, water will not form a

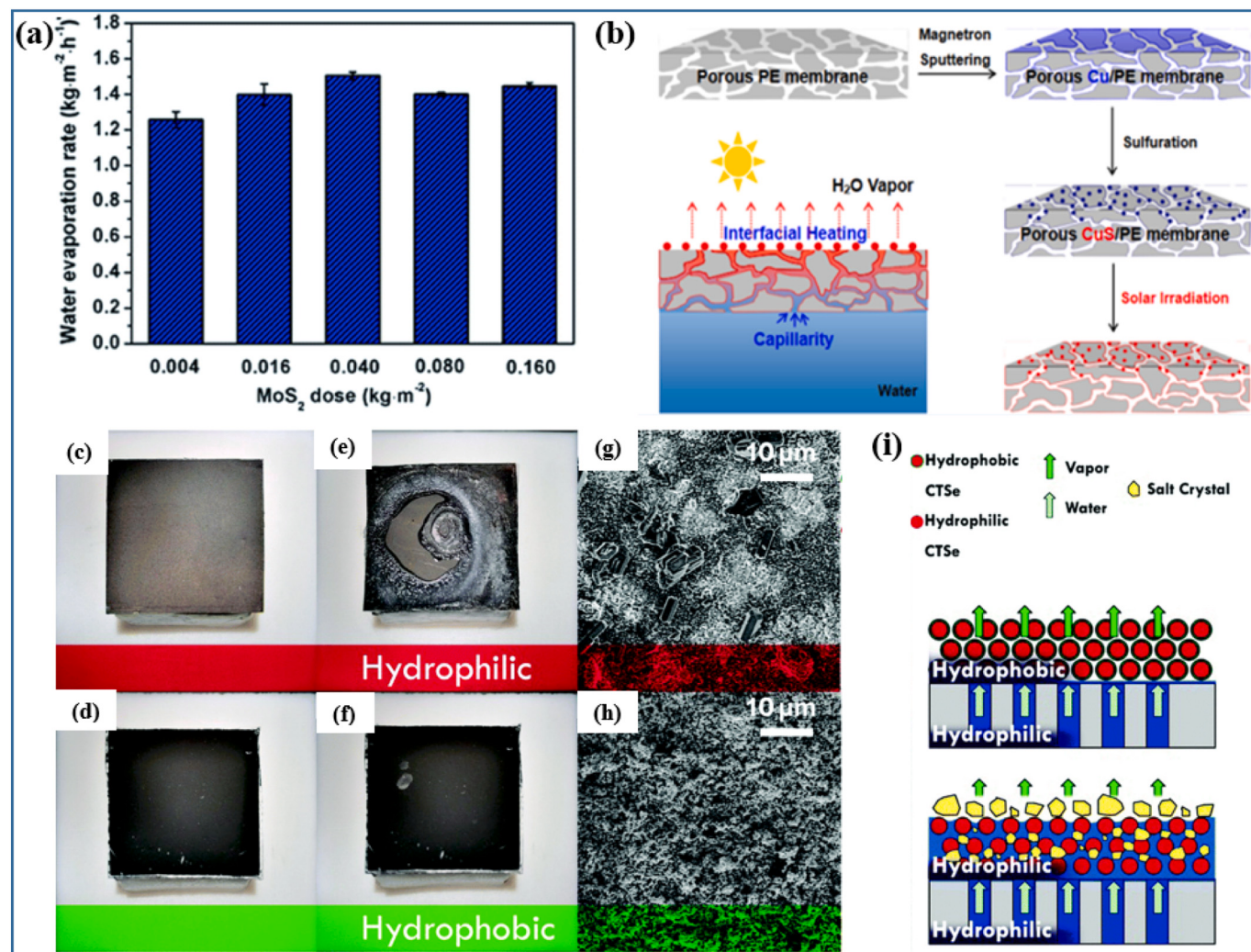


**Fig. 7.** (a) Effects of  $\text{MoS}_2$  concentrations on water evaporation [97], (b) schematic illustration of fabrication process of CuS on porous polyethylene membrane and the water evaporation mechanism [42], (c and d) hydrophilic and hydrophobic membranes before and (e and f) after 10 h solar desalination, (g,h) SEM images of the hydrophilic and hydrophobic membranes after test, (i) schematic illustration of the salt resistance of the two types of membranes [109].

hydration layer on the surface; thus, salt deposition is diminished [109,117]. As many semiconductor materials exhibit hydrophilicity, they need to be surface treated to become hydrophobic and, commonly, silane treatment is employed [118–121]. For example, Ye et al. modified TiO<sub>x</sub>-coated on stainless steel (SS) meshes with 1H,1H,2H,2H-perfluorooctyltrichlorosilane (PFOTS) through vapor deposition and produced a superhydrophobic surface with a contact angle of 150° [122]. The modified hydrophobic membrane surface exhibited a stable, non-fouled surface after solar irradiation for days. Que. and his co-workers observed that the salts crystallized and accumulated on hydrophilic Cu<sub>2</sub>SnSe<sub>3</sub>/hydrophilic cellulose membrane resulted in a lower water evaporation rate (Fig. 7c-h) [109]. On the other hand, the hydrophobic Cu<sub>2</sub>SnSe<sub>3</sub>/hydrophilic cellulose membrane surface maintained clean and unclogged even after 10 h of operation, with continuous water evaporation through the channels made by interconnected nanospheres. The proposed mechanism of water evaporation channel and salt rejections is illustrated in Fig. 7i. The use of hydrophobic semiconductor PTMs is not sufficient strategy to mitigate the salt crystallization. Some strategies involve specially-designed hydrophobic water channels within the substrate, instead of making the whole substrate hydrophobic, so as to allow only water vapor to pass through rather than water wicking to the top that can bridge salt transport as well. However, the design of such microchannels is challenging and should be further investigated in the future. Hydrophilic microsize substrates such as biomass can also display great potential to mitigate salt crystallization issues through self-cleaning, which needs further exploration in combination with semiconductor nanostructure materials [123]. The integration of nano-size semiconductor materials to these types of substrate might be advantageous for SSG. Table 2 gives a summary of the different semiconductor-based PTMs reported in literature and their SSG performance.

#### 4. Application of semiconductor PTMs in water purification

##### 4.1. Desalination

Free and abundant solar energy is a promising renewable energy source for seawater desalination. A scaled-up SSG device can obtain adequate potable water from seawater for daily drinking needs [33,144–146]. To achieve such a goal, SSG experiments have been often conducted using either simulated or real seawater. Usually, the produced distilled water from SSG devices surpasses the drinking water standards set by the World Health Organization (WHO) and the US Environmental Protection Agency (EPA).

Some of the notable results on seawater desalination work using semiconducting PTMs devices were proposed. For example, Luocai's group designed and fabricated an SSG device utilizing a black amorphous Al-Ti-O nanostructure as PTM, which could generate a sufficient amount of water with a production rate  $\sim 4 \text{ L m}^{-2} \text{ day}^{-1}$  [93]. In another study, a group demonstrated the large-area fabrication of hollow black TiAlO<sub>x</sub>/PVDF nanocomposites (Fig. 8a,d) [111]. The work reveals the desalination of artificial seawater with NaCl concentrations of 8.3 wt%, 15.3 wt%, and 26.5 wt% (Fig. 8e,f). The outdoor experiments were conducted at 21 °C and relative humidity of 65%. As illustrated in Fig. 8b and c, they invented automatic sunlight tracking solar energy evaporator for desalination, with a box that rotates automatically around a shaft to track the sunlight to obtain the maximum sunlight intensity during the day. After the desalination process, the concentrations of the Na<sup>+</sup> ions were found to be below the detection limit even lower than the WHO and US EPA standards concentration. Furthermore, the desalination of 15 wt% NaCl produced 4.0 L m<sup>-2</sup> day<sup>-1</sup> of pure water. The total cost of TiAlO<sub>x</sub> and PVDF membrane was calculated to be \$13.44/m<sup>2</sup>, which is considered as cost-competitive compared to other noble metals based PTMs. Jijian et al. designed and fabricated a device consisting of a left chamber size of 20 cm × 20 cm with plasmonic Cu/Graphene membrane for solar-driven water desalination (Fig. 9c) [125]. Through the covered transparent glass plate, the evaporated water vapor

is condensed into liquid and collected at the right chamber. The desalination experiment was conducted with a 5 wt% NaCl stained with black ink. The ICP-OES analysis indicated that only 1.08 mg L<sup>-1</sup> NaCl residue was identified after the desalination process (Fig. 9b), demonstrating that the collected water is potable. An outdoor experiment conducted under natural solar illumination for 3 days generated up to 600 mL of clean water.

Shang et al. reported the applications of CuS/PE membrane for solar-driven water desalination [42]. The inclination angle of the glass cover was 10°, and the fan was driven by a solar panel to simulate the natural wind to speed up the flow of condensed water. The fan assists the collection of condensed water by the collecting chamber through the hole, as shown in Fig. 9a. Yang et al. fabricated a device consisting of semiconducting PTMs such as CuSnSe<sub>2</sub> deposited on mixed cellulose esters as a support membrane. They used seawater from the Bohai Sea, Qinghai Lake, and Caka Salt Lake. After the desalination process, the concentration of four ions Na<sup>+</sup>, K<sup>+</sup>, Ca<sup>2+</sup>, and Mg<sup>2+</sup> were significantly decreased with salt rejection beyond 99.5%, which was below the WHO and EPA standards [109].

##### 4.2. Wastewater treatment

Besides seawater desalination, semiconductor PTMs were extended to industrial waste treatment such as organic contaminants (i.e., dyes, volatile pharmaceutical compounds) and heavy metals removal. The organic dyes degradation could be achieved by absorbing sunlight using the PTMs, followed by evaporation and condensation of clean water, leaving the contaminants behind. For example, Chen et al. investigated the MoS<sub>2</sub> based solar evaporator system as a reductant for organic compounds. MoS<sub>2</sub>/ALP revealed the efficient removal of organic pollutants by the photocatalytic oxidation process. Nitrobenzene, carbamazepine, and naproxen were used as model pollutants with initial concentrations of 400, 472.5, and 460.5 µg/L, respectively. After the evaporation process, the contaminants were effectively reduced to 74.3, 51.5, and 19.1 µg/L, respectively [97]. They also investigated real seawater samples (obtained from the East China Sea), analyzing the total organic carbon (TOC) of the samples before and after the photodegradation processes. The TOC results revealed that the concentration was reduced from 9.60 to 3.77 mg L<sup>-1</sup>. Furthermore, other organic pollutants like tryptophan and humic acid were also decreased significantly after the solar-driven photodegradation process. Besides the mentioned catalyst, other devices also exhibited excellent performance for organic contaminants removal. For instance, CuSnSe<sub>2</sub>/mixed cellulose ester showed a 100% rejection of Rhodamine B (RhB), methyl orange (MO), and methyl blue (MB) dyes [109]. It has been reported that the PTMs generate highly reactive species after absorbing the sunlight, which further reacts with organic species to dissociate the organic bonds into small and nontoxic molecules [40]. For example, the activation of CuO nanowires, through adding potassium monopersulfate (PMS) into the polluted water with MO showed great potential to photodegrade MO with a removal efficiency of more than 90% within 20 min under light illumination, as shown in Fig. 10a–c. [40]. The high removal is attributed to the activation of PMS by the CuO nanowires at the top surface and bulk water after solar irradiation. This excellent performance motivated them to investigate the performance using industrial wastewater. The TOC analysis results indicated that 58% reduction in organic contaminants was observed after 8 h due to the excellent photocatalytic behaviour of CuO nanowires mesh.

Heavy metals are non-degradable, and they can accumulate in living tissues, causing various diseases and disorders. For this reason, their removal is necessary before discharging them as wastewater [147]. Therefore, heavy metal drinking water levels should be below 2 ppb, according to the US Environmental Protection Agency (EPA) [148]. Up-to-date, few reports demonstrated the application of using semiconductors PTMs for the removal of heavy metals. For instance, Li et al. revealed the efficiency of MoS<sub>2</sub>/C PU sponge for removing Ni ions with

**Table 2**

The synthesis and characteristics semiconductor PTMs and their SSG performance.

Photothermal materials characteristics				Performance			Ref.
Photothermal materials	Substrate/thermal insulator	Synthesis method	Morphology/size/surface area	Light absorption (%)	Water evaporation efficiency (%) under one sun	Water Evaporation rate ( $\text{Kg m}^{-2} \text{ h}^{-1}$ ) under one sun	
Plasmonic semiconductor							
Multifunctional CuO nanowire mesh	Copper foam/EPE	Immersion + Alcohol burner	Nanowires on Cu mesh	93	84.4	1.42	[40]
3D-plasmonic covellite CuS hierarchical nanostructure/PVDF	PVDF/self-float	Hydrothermal + phase inversion	Hierarchical nanostructure composed of nanoplates T: 85 nm	>90 UV-vis >96 NIR	90.4 ± 1.1	1.43	[96]
CuS nanoflower	SCM/self-float	Hydrothermal	3D covellite nanoflower composed of nanosheets/D: ~2 $\mu\text{m}$ /CuS NPs D: ~40 nm/PE PS: ~73.9 $\mu\text{m}$ , T: 112 $\mu\text{m}$	–	68.6	1.09	[55]
Single-layer CuS/PE membrane	PE - self-float	Solvothermal	CuS NPs D: ~40 nm/PE PS: ~73.9 $\mu\text{m}$ , T: 112 $\mu\text{m}$	93	63.9	1.02	[42]
Cu NPs/C-TiO <sub>2</sub>	SiO <sub>2</sub> -self-float	Microfluidic jet spray drying	Microparticles with a wrinkled surface (S: 95 $\mu\text{m}$ ) and hollow inside with a thin shell (~10 $\mu\text{m}$ ) coated carbon with PS: 4.1 nm	–	92.2	1.5	[124]
Cu <sub>x</sub> S film	MCE/PU foam	Solvothermal	Granular structure	85	~80 ± 2.5	1.12	[110]
Cotton-CuS yolk-shell nanocage-agarose aerogel	Cotton-PS foam	Casting method + freeze-drying	Shell wall T: 40–70 nm	94–95.5	94.9	1.63	[112]
3D hierarchical architecture Cu <sub>x</sub> S/Cu foam	PS foam	Solution-based method	Nanorods to 3D hierarchical structure	96.3	94.5	1.96	[105]
Cu <sub>2</sub> SnSe nanosphere array	CEM/PS foam	Reflux	Nanosphere array/D: 200–300 nm	97	86.6	1.657	[109]
Cu <sub>2</sub> ZnSnSe nanosphere array				95.5	85.7	1.643	
Cu <sub>12</sub> Sb <sub>4</sub> S <sub>13</sub> nanoparticles	CAM/Self-float	Reflux	NPs/S: 30–70 nm	–	–	6.6	[117]
Copper nanodot-embedded N-graphene urchins	Self-floated	Reflux-oxidation + annealing	Nanodot embedded into Uniform urchin like nanostructures of 3D self-assembled/NG T: 5 nm	99	82	0.63	[125]
CuCr <sub>2</sub> O <sub>4</sub> /SiO <sub>2</sub> composite	Quartz glass fibers/EPS	Impregnation + calcination	Aggregated particles on nonwoven fibrous membrane	75-vis 44-NIR	–	1.32	[126]
Ultralong Cu <sub>2-x</sub> S nanowire	Melamine foam	Polyol method	Ultralong nanowire/D: ~50 nm and L: tens of micrometers	–	89.9/8 sun	–	[127]
2D layered materials							
2D MXene	PVDF/PS foam	Etching + ultrasonic exfoliation	Layered MXene Flakes/S: 500 nm	–	84	–	[22]
3D MXene Melamine foams architectures	Melamine-EPE foam	Etching + sonication + dip-coating+	Ultrathin and transparent nanosheets	98	88.7	1.41	[108]
Hydrophobic MXene/MCE	MCE-PS foam	Etching + ultrasonic exfoliation	Layered structure with wrinkles by tightly stacking nanosheets	–	71	1.31	[102]
Biomimetic Mxene	PS foam	Etching + ultrasonic exfoliation	Crumpled structure	93.2	86.7	1.33	[87]
MoS <sub>2</sub> nanosheets	BNC hydrogel-self-float	Chemical exfoliated+	Nanosheet T: 1.5 ± 0.7 nm, with lateral dimensions of 200–800 nm	96	76/0.76 sun	0.81/0.76 sun	[82]
MoS <sub>2</sub> /C-polyurethane composite	Polyurethane	Hydrothermal	3D spoke-like structure	98	94	1.95	[41]
SWNT Film -MoS <sub>2</sub>	Self-floated	Chemical vapor deposition + hydrothermal	SWNT: 2D porous network structure, MoS <sub>2</sub> : wrinkles flower-like nanosheets P S between SWN film and MoS <sub>2</sub> : 20–200 nm, T: 120 nm. MoS <sub>2</sub> T: 5 nm.	82	91.5/5 sun	6.6/5 sun	[98]
Nanoflowers MoS <sub>2</sub> on ALP	ALP/EPE	Hydrothermal	Nanoflower composed of numerous nanosheets	96.15	80	1.27	[97]
3D dimpled 2H MoS <sub>2</sub>	PES/PS sheet	Exfoliation + microwave + annealing + solar irradiation	3D dimpled with open macroporous (1–2 $\mu\text{m}$ ) network	80–90	461 LMH/bar	83.8	[25]
PEGylated MoS <sub>2</sub> -cotton cloth	Cotton cloth/PS foam	Hydrothermal	Hierarchical nanoflower layers	90	90 ± 3.5	1.3	[128]
Oxygen deficient metal oxide							
W <sub>18</sub> O <sub>49</sub> /carbon foam composite	Carbon foam	Hydrothermal + annealing	Nanowires aggregated and interweave into porous net	–	–	1.694	[73]
WO <sub>2.72</sub> /polylactic acid fiber membranes	Polylactic acid fiber membranes self-float	Melt electrospinning	Nanoparticles	–	81.39	3.81	[32]

(continued on next page)

**Table 2 (continued)**

Photothermal materials characteristics				Performance			Ref.
Photothermal materials	Substrate/ thermal insulator	Synthesis method	Morphology/size/surface area	Light absorption (%)	Water evaporation efficiency (%) under one sun	Water Evaporation rate (Kg m <sup>-2</sup> h <sup>-1</sup> ) under one sun	
Quasi-metallic WO <sub>2.9</sub> nanorods	CM- Self-float	Hydrothermal + calcination+	Nanorods D: 25 nm, L: 50 nm	90.6	81	1.28	[129]
2D defective WO <sub>x</sub> nanosheets	PE foam	Hydrothermal + calcination + exfoliation	2D nanosheets/S: 150 nm/T: 5 nm	90	78.6	–	[130]
W <sub>18</sub> O <sub>49</sub> mesocrystal/ PDMS	PTFE/PDMS-self-float	Solvothermal + flow-through	No difference on morphology of mesocrystal W <sub>18</sub> O <sub>49</sub> after adding PDMS	–	82	1.153	[74]
WO <sub>3-x</sub> nanorods decorated wood	Wood	Hydrothermal + annealing	Nanorods with D: 10 nm is distributed uniformly on wood	94	82.5	1.28	[65]
WC nanoarray on carbon fiber paper	PTFE/self-float	Hydrothermal + annealing	Nanoarray composed of NPs uniformly grow on CC/T: 10–20 nm	97.5	90.8	1.1	[131]
Oxygen-defected molybdenum oxides hierarchical nanostructure	EPE	Hydrothermal	Flower like structure composed of nanosheet/S: 1 μm	97	85.6	1.255	[75]
MoO <sub>3-x</sub> quantum dots	CAM- self-float	Hydrothermal	Uniform and monodispersed quantum dots	–	62/5 sun	4.95/5 sun	[132]
Metal-doped semiconductor							
Pt/Au/TiO <sub>2</sub> -decorated plasmonic wood carbon	Carbonized wood - self-float	Calcination	NPs/S: 500 nm	–	90.4/10 sun	–	[133]
Au-ZnO	CEM/self-float	Sonication + chemical reduction	Hedgehog-like hierarchical ZnO particles/Au NPs	–	–	8.70/10 sun	[134]
TiAlON nanocomposite on porous NiO disk	NiO disk/self-float	Cathodic arc deposition	P S: of NiO 2 μm and NiO particles with P S: <200 nm	97	73	1.13	[135]
Ni NPs decorated TiO <sub>2</sub> nanotube array	Ti foil/closed-cell foam	Anodization + electrodeposition	Ni NPs decorated honeycomb titanium dioxide nanotube TNT array/TNT D: 150–200 nm/NPs D: 40 nm	96.83	78.9	–	[88]
Ag/TiO <sub>2</sub> core-shell NPs	PU foam	Chemical reduction	Ag D: 19.7 ± 1.4 nm, TiO <sub>2</sub> T: 2.2 ± 0.7 nm	–	53.6	0.86	[90]
Black amorphous Al-Ti-O nanostructure/ PVDF	PVDF/self-float	Ball milling + etching + phase inversion	Agglomerated uniform structure/ SA: 35.17 m <sup>2</sup> g <sup>-1</sup>	90.23	77.52	1.24	[111]
Hollow black TiAlO <sub>x</sub> nanocomposites/ PVDF	PVDF/self-float	Annealing + etching + phase inversion	Hollow structure	90.2	71.1	1.17	[93]
Other types of semiconductor							
Nanosized titanium sesquioxide (Ti <sub>2</sub> O <sub>3</sub> )	CM/self-float	Ball milling	Nanoparticles with D: 400 nm	92	<65%	1.32	[95]
Black titania nanocage/ PVDF	PVDF/self-float	Molten salt assisted self-assemble + phase inversion	Nanocage S: 70 nm with interconnected nanograins S: 15 nm and mesopores of 4–10 nm, SA: 255 m <sup>2</sup> g <sup>-1</sup>	–	70.9	1.13	[111]
Black TiO <sub>x</sub> NPs	SS mesh - self-float	Mg reduction + Spin coating	NPs S: 24 nm/T: 6 nm	91.3	50	0.8012	[122]
C-TiO <sub>2</sub> 3D honeycomb CuFeMnO <sub>4</sub>	PVA - self-float PS foam	Sol-gel + spin coating Impregnation + annealing + photo-fenton reaction	NPs on amorphous carbon Honeycomb ceramic with the coating layer	83.7 97.5	77.83 91	1.24 1.45	[136] [137]
Co <sub>3</sub> O <sub>4</sub> nanoforest/NF	NF/EPE foam	Hydrothermal + calcination	Flower like structure composed of nanoscale needles	96.27	84.45	1.226	[138]
Co <sub>2.67</sub> S <sub>4</sub>	PTFE-self-float	Solvothermal	NPs (S: 8–15 nm) agglomerated into large particles (200–300 nm)	–	82/2 sun	2.26/2 sun	[120]
Fe <sub>3</sub> O <sub>4</sub> magnetic NPs	ALP - self-float	Dip coating + chemical method	NPs attached on rGO	95	75	–	[139]
Ni-NiO <sub>x</sub>	NF-self-float	Hydrothermal + calcination	NPs (D: 300 nm) on nanosheet	90	94	1.45	[140]
SnSe@SnO <sub>2</sub> core-shell nanocomposite	Nylon film - self-float	Reflux + oxidation	Core-shell nanocomposite	–	75.3	1.19	[141]
Fe <sub>3</sub> O <sub>4</sub> /C core-shell nanostructures	Self-float	Solvothermal	Core shell composed of nanosphere coated with carbon	90.32	67	1.07	[118]
3D porous Cu foam	CuF/PDMS	Oxidation + salinization	Rough surface with needle-like nanostructure	93 (T)	48	1.584	[142]
Bi <sub>2</sub> S <sub>3</sub> /PVDF composite	PVDF/PU	Solvothermal + phase inversion method	Chrysanthemum-like architecture	97	92.9	1.66	[143]

S: Size, P S: pore size, PD: Pore diameter, T: Thickness, D: Diameter, L: Length, NPs: Nanoparticles, NCs: Nanocages, EPE: Expandable polyethylene, EPS: Expandable polystyrene, PE: Polyethylene, PDMS: Polydimethylsiloxan, PS: Polystyrene, PU: Polyurethane, CEM: Cellulose ester membrane, CM: Cellulose membrane, PTFE: Polytetrafluoroethylene, PES: Poly(ether sulfone), PVDF: poly(vinylidene fluoride), PVA: Polyvinyl acetate, SCM: Semipermeable collodion membrane, CAM: Cellulose acetate membrane, BNC: Bacteria nanocellulose, rGO: reduced graphene oxide, CNT: Carbon nanotube, SWNT: Single-wall carbon nanotube, NF: Nickel foam, AAM: Anodized alumina membrane, SS: Stainless steel.

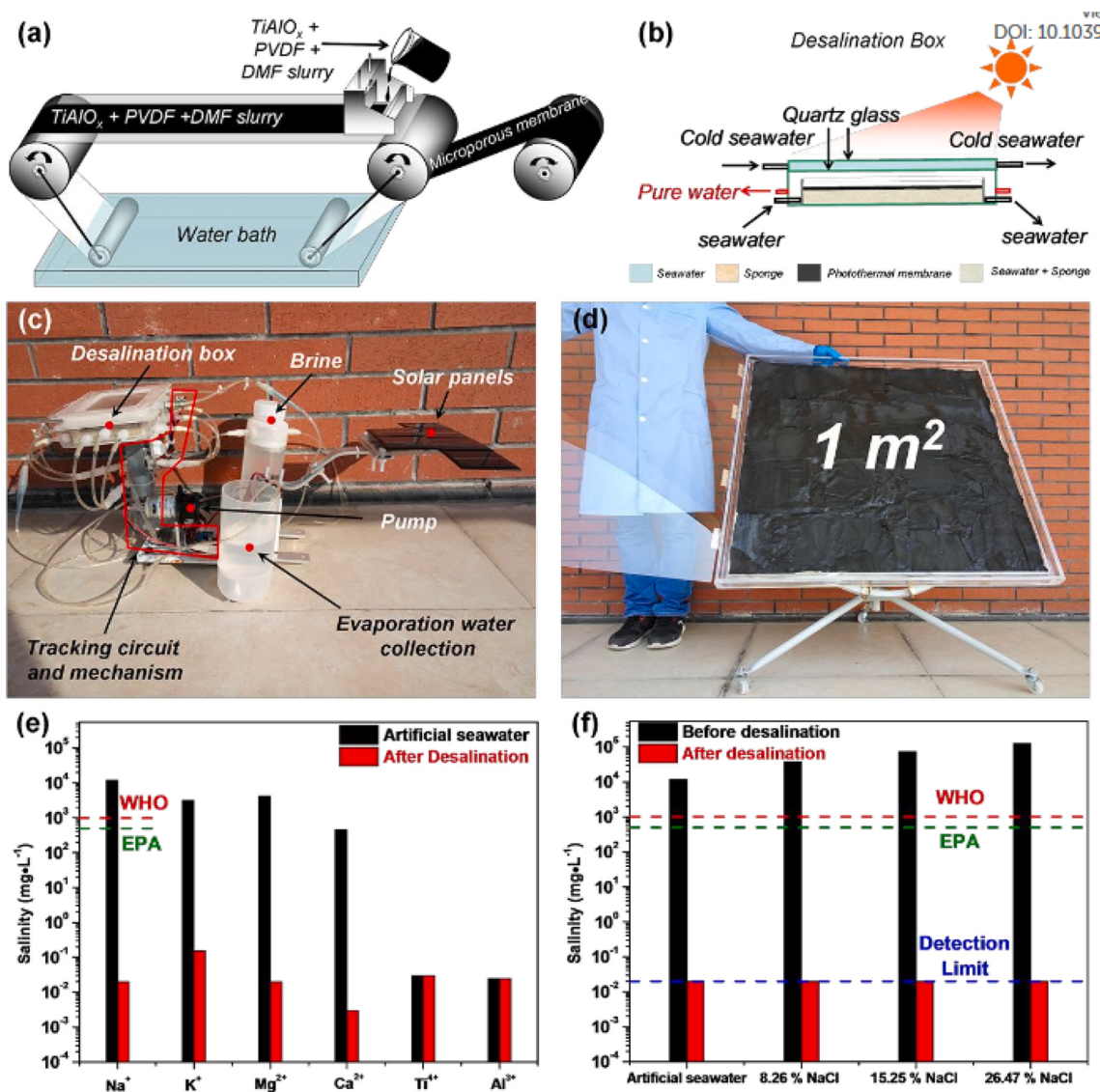


**Fig. 8.** (a) Schematic of the tape casting technology for large-scale production of membrane for SSG, (b) schematic of the desalination box for automatic tracking solar desalination system, (c) design of an automatic tracking solar desalination system, (d) photo of a manual tracking solar desalination system, (e) concentrations of ions before and after desalination, and (f) concentrations of  $\text{Na}^+$  in four different water samples before and after desalination [93].

high efficiency (~99.6%) after a one-step SSG process, as shown in Fig. 10d and e [41]. The mercury removal efficiency was also conducted by mixing the microbeads made of  $\text{MoS}_2/\text{C}$  with 200 ppb Hg from water, close to the level of real wastewater. The microbeads made of  $\text{MoS}_2/\text{C}$  could remove mercury levels up to 1 ppb level upon sunlight illumination. This is attributed to the hydrothermally synthesized  $\text{MoS}_2/\text{C}$  containing  $\text{H}^+$  ions ( $\text{H}_x\text{MoS}_2/\text{C}$ ) that could exchange with ionic  $\text{Hg}^{2+}$  and formation of strong Hg-S bonding. In contrast, Guo et al. demonstrated the effectiveness of PEGylated  $\text{MoS}_2$ -cotton cloth to remove mercury to below 2 ppb [128]. These results illustrate the efficiency of  $\text{MoS}_2$  based PTMs for the removal of mercury.

#### 4.3. Recyclability and stability of photothermal materials

Recyclability and stability of PTMs play a vital role in affecting the real field implementation of the SSG device and determine their cost-effectiveness. Therefore, PTMs should be able to undergo many use cycles while maintaining acceptable levels of device performance. Inorganic semiconductor materials demonstrated excellent stability, reusability making them a promising material for practical application. For instance, Luocai et al. investigated the stability of a black Titania membrane under high salinity ( $\text{NaCl}$  15.3 wt%) solution by studying the morphology and surface area change after 5 days of operation. The SEM images revealed no difference in morphology and structure, indicating its good long term stability. Meanwhile, the BET surface area analysis showed a slight change in the porosity from  $9.38$  to  $12.54 \text{ m}^2 \text{ g}^{-1}$ .

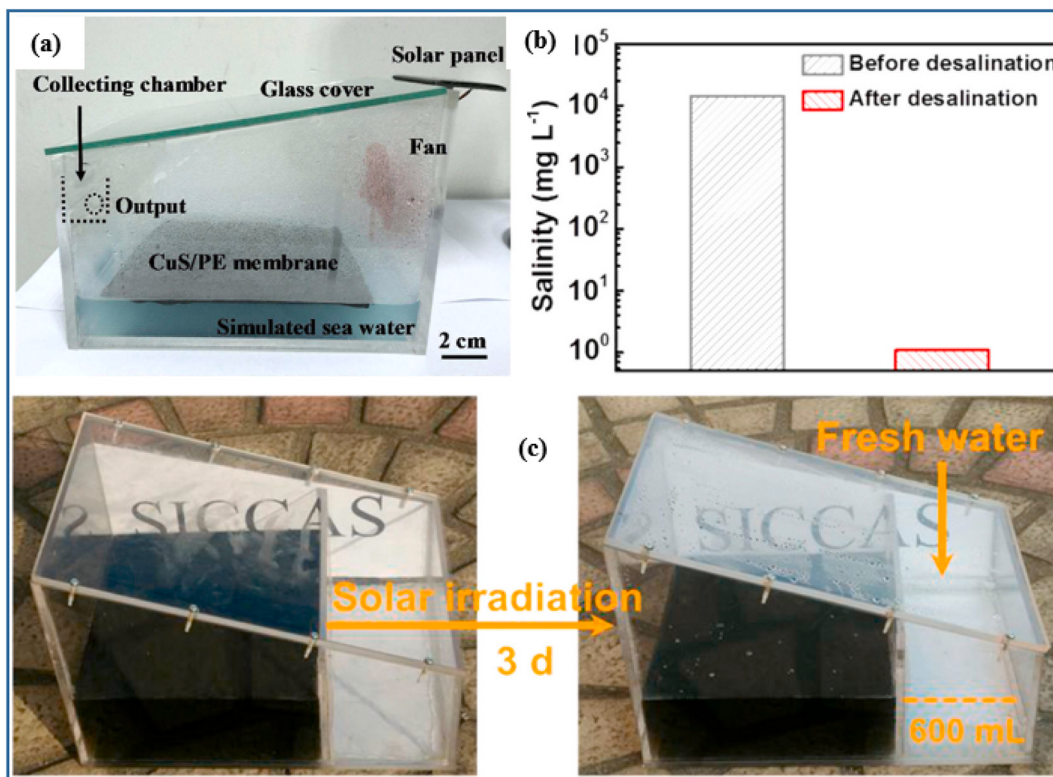


**Fig. 9.** (a) Photograph of the point-of-use device for direct and all-in-one solar distillation [42]; (b) salinity comparison before and after solar desalination, and; (c) a solar desalination device for real field application [125].

Additionally, no apparent salts were accumulated on the membrane after 5 cycles of the desalination process, which shows its excellent stability. Layered SnSe deposited on nickel foam has proven to be reusable by just removing it from the aqueous solution over several cycles without any performance decay, showing its material stability and reusability [99]. CuFeMnO<sub>4</sub>/honeycomb ceramic-based heterogeneous photo-Fenton system prevents the formation of iron sludge by immobilizing iron oxides compare to the heterogeneous iron salts and enables its reusability by simple flushing, MB degradation efficiency was effectively maintained for 20 cycles [137]. Moreover, the concentrations of Cu, Fe, and Mn were negligible in the distilled water, demonstrating excellent stability in water. The stability of MoS<sub>2</sub> loaded on air-laid paper was examined by floating it on the water surface for a period of seven months with a solar evaporation test conducted at different time intervals. The evaporation rate was stable for 13 cycles for 210 days, demonstrating its excellent durability and stability [97]. Han et al. realized that the salt crystals on the surface of WC nanoarray on carbon fiber paper could be removed via washing with original saline water (3.5% NaCl) [131]. WC nanoarray on carbon fiber paper displayed excellent solar efficiency and cycling stability for 100 cycles (1 h per cycle) and a water evaporation rate of 1.1 kg m<sup>-2</sup> h<sup>-1</sup>. ICP-MS elemental analysis was used to evaluate the material stability of CuSnSe<sub>2</sub> on mixed cellulose ester. The analysis results indicated that a negligible amount of copper or selenium was found in the vapor or in the bulk seawater. Another group conducted investigations on the stability and recyclability of CuO nanowires on copper foam. A stable water evaporation rate of  $1.42 \pm 0.08$  kg m<sup>-2</sup> h<sup>-1</sup> was achieved for a period of three days. Furthermore, with a combination of PMS, the recyclability after removal of MO was conducted in the dark, and removal of 84% was achieved under continuous repeated 5 cycles [40]. Interestingly, they found that after 8 h of illumination, no copper ions were detected in the distilled water, and the minute concentration of copper ions were released ( $0.0027$  mg cm<sup>-2</sup> h<sup>-1</sup>) through the evaporation process, acting as a bacteria inhibitor on both material surface and the bulk water. Table 3

presents more details on the stability and durability of semiconductor PTMs.

## 5. Conclusion and perspectives

Increasing interest in SSG for water purification in recent years has been mainly due to advancements in PTMs, better understanding and approach for thermal management, and newer system and process configurations. Semiconductor PTMs have been targeted due to: (i) many semiconductor materials exhibit low-material costs and many cases involve simple, easy synthesis or modification processes; (ii) can be designed and formed in diverse morphologies, shapes, and sizes; (iii) they have excellent light absorption characteristics, (iv) high photothermal conversion efficiency; and (v) remarkable SSG performance toward desalination and wastewater treatment. This review has thoroughly discussed the contribution of semiconductor PTMs for solar steam generation applications including various synthesis approaches, techniques on improving their photothermal properties, thermal management strategies, and their utilization for desalination and wastewater treatment. Review of the literature indicated that 3D solar steam generators could achieve water evaporation efficiency and production compared to a 2D SSG system. Among the semiconductors reported for SSG, copper sulfide is the most commonly used, demonstrating superior performance in both wastewater treatment and seawater desalination. The growing of semiconductor PTMs on a metal substrate such as 3D metal foams has shown better performance than polymeric membrane substrates.

Despite the outstanding achievements in semiconductor PTMs for SSG, some issues still need to be addressed to bring this technology to real-world applications. Future efforts in this field should be focused on;

- (i) **Enhancing solar conversion of semiconductor materials.** There is a need to develop innovative microstructure semiconducting PTMs. This will not only enhance the light absorption but also to

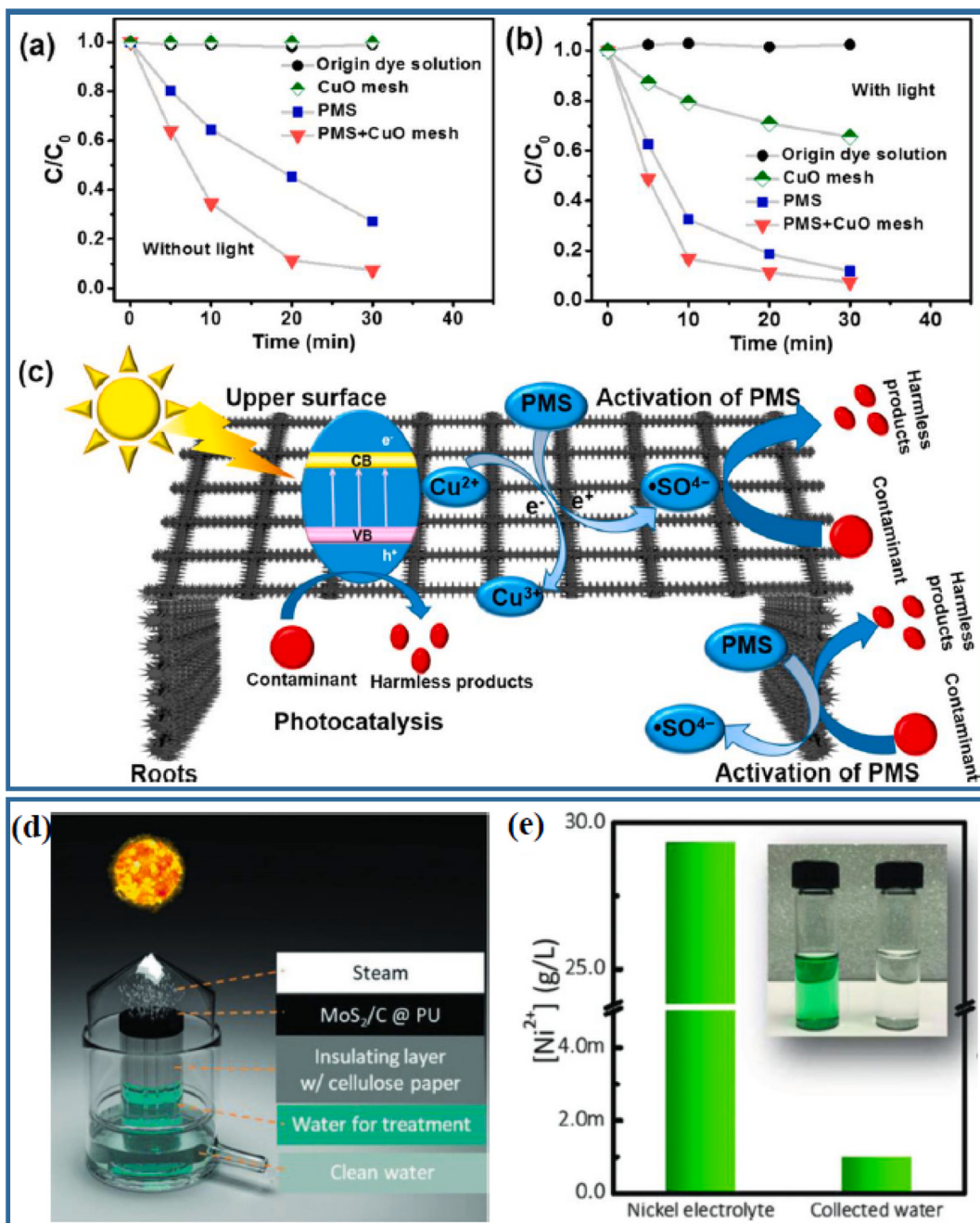


**Fig. 10.** (a), (b) MO removal in dark and with solar irradiation under different conditions, (c) schematic for multifunctional CuO nanowire mesh in contaminant degradation [40], (d) photograph of an SSG system for testing of water quality and ion removal, and (e) the concentration of nickel ions before and after purification by SSG (inset: original nickel-containing solution (left) and water after the SSG process (right)) [41].

- localize the heat and facilitate the water to escape fast, and consequently lead to excellent water evaporation efficiency. Nanocomposite semiconductor with conjugated polymer (e.g., polypyrrole and polyaniline) to further enhance the light absorption, and photothermal conversion efficiency should be thoroughly explored in the near future.
- (ii) **Effective substrates for semiconductor PTMs.** The support substrates are known to play an effective role in suppressing heat loss, enhancing water transport and anti-salt crystallization features in SSG. Based on this literature study, there is still a lack of investigations on the substrates used. Future research should consider these directions by integrating the as-designed semiconductors nano/microstructure with suitable substrates such as

biomass materials (e.g., biomass-driven hydrogel, microchannel biomass) or conjugated hydrogel polymers.

- (iii) **Designing semiconductor PTM devices based on 3D design.** In the past three years, increasing studies revealed that developing 3D SSG devices can produce exceptional water evaporation performance, even exceeding the theoretical values. However, the exact working mechanism is still not clear. Thus, there is a need further do in-depth studies on its potential and process. More efforts should also be made to design 3D isolated structure that proves to be a fantastic approach to restrict heat loss and harvest energy from the environment that could contribute to increasing the system efficiency.

**Table 3**

The stability and the performance of semiconductor PTMs devices in water purification.

Photothermal materials	Water source + location	Materials costs/prototype costs	Salt concentration/ evaporation performance	Pollutants	Distilled water production rate	Durability test	Stability test	Ref
Porous CuS NPs on PE hybrid	–	–	Na <sup>+</sup> , K <sup>+</sup> , Mg <sup>2+</sup> , Ca <sup>2+</sup>	–	–	PTMs can be recycled: 20 times	–	[42]
Cu NPs/C-TiO <sub>2</sub>	Artificial sea water + lab scale	–	3.5% NaCl	–	With solar UV: 0.6 kg m <sup>-2</sup> h <sup>-1</sup> With ViS light irradiation: 1.1 kg m <sup>-2</sup> h <sup>-1</sup>	100% performance sustainment after 10 cycles	No change in the morphology observed.	[124]
	Simulated sea water + Soochow, China 28th June 2019	–	–	–	Under natural sunlight at 0.5 kg m <sup>-2</sup> h <sup>-1</sup>	–	- Temperature increased from 15 °C (without PTMs) to 32 °C (with PTMs).	
Cotton-CuS yolk-shell nanocage-agarose aerogel	Semaphore Beach, Adelaide, Australia	–	Na <sup>+</sup> , K <sup>+</sup> , Mg <sup>2+</sup> , Ca <sup>2+</sup> Salt conc: 0.54 ppm	–	ER: 1.03 kg m <sup>-2</sup> h <sup>-1</sup> over 5 h	Stable performance 15 cycles and excellent chemical stability (5 h)	Sample weight almost unchanged Copper conc. in 1st cycle and 15th cycle are 6.25 ppb and 6.90 ppb	[112]
3D hierarchical architecture Cu <sub>x</sub> S/Cu foam	South china seawater	–	At Open system ER: 2.69 kg m <sup>-2</sup> h <sup>-1</sup> (Wind energy and net energy) (Na <sup>+</sup> , Mg <sup>2+</sup> , K <sup>+</sup> , and Ca <sup>2+</sup> ) decrease from 9038.7, 1259.6, 544.1 and 426.0 mg L <sup>-1</sup> to 1.24, 0.11, 0.25 and 0.27 mg L <sup>-1</sup>	Organic dyes (Sudan III dyed, MB)	5.2 L m <sup>-2</sup> day <sup>-1</sup> in a 30-day consecutive outdoor	1.73 kg m <sup>-2</sup> h <sup>-1</sup> after 13 days (10 h/day)	–	[105]
Cu <sub>2</sub> SnSe nanosphere array	Bohai Sea, Qinghai Lake and Caka Salt Lake	–	Na <sup>+</sup> , K <sup>+</sup> , Mg <sup>2+</sup> , Ca <sup>2+</sup>	Heavy metals (Fe, Cu, Cr) Organic dyes (RhB, MO, MB)	–4 h evaporation: 15 mL water obtained; 45.2% of the theoretical value. After 8 h evaporation: 15 mL water obtained; 53.7% of the theoretical value –100% rejection in organic dyes and heavy metals Salts conc. below WHO, EPA, membrane based and distillation based seawater desalination technologies	20 cycles (1 h/cycle)	No Cu and Se were observed in either the vapor or the bulk water (8 h)	[109]
Copper nanodot-embedded N-graphene urchins	Artificial sea water	–	5% NaCl 1.08 ppm of NaCl remain.	–	- ER: 0.63 kg m <sup>-2</sup> h <sup>-1</sup> , namely ~5 L m <sup>-2</sup> day <sup>-1</sup> was achieved under natural sunlight	Stable efficiency for 10 cycles (5 h/cycle)	–	[125]
Black titania nanocage	East Sea, China	–	Na <sup>+</sup> , K <sup>+</sup> , Mg <sup>2+</sup> , Ca <sup>2+</sup> , B <sup>3+</sup>	–	Highly reduction of metal cations, meanwhile Mg <sup>2+</sup> , B <sup>3+</sup> were below ICP-OES detection level	Stable evaporation rate for 7 days 10 cycles (5 h/cycle)	Mg <sup>2+</sup> , B <sup>3+</sup> below detection limit of ICP-OES	[149]
Hollow black TiAlO <sub>x</sub> nanocomposites	Artificial sea water	11.17 \$/m <sup>2</sup>	Na <sup>+</sup> , K <sup>+</sup> , Mg <sup>2+</sup> , Ca <sup>2+</sup> ER: 0.49 ± 0.1 kg m <sup>-2</sup> h <sup>-1</sup>	–	4–5 L m <sup>-2</sup> day <sup>-1</sup> (8 h/day) under natural sunlight	10 cycles (1 h/cycle)	Ti <sup>4+</sup> , Al <sup>3+</sup> below detection limit of ICP-OES	[111]
Black amorphous Al-Ti-O nanostructure/PVDF	Artificial sea water	13.44 \$/m <sup>2</sup>	8.3 wt%, 15.3 wt%, 26.5% NaCl	Na <sup>+</sup> , K <sup>+</sup> , Mg <sup>2+</sup> , Ca <sup>2+</sup> Six orders of	4 L m <sup>-2</sup> day <sup>-1</sup> (8 h/day) under natural sunlight	Production of 4 L m <sup>-2</sup> day <sup>-1</sup> maintain stable for 5 days	Ti <sup>4+</sup> , Al <sup>3+</sup> below detection limit of ICP-OES	[93]

(continued on next page)

**Table 3 (continued)**

Photothermal materials	Water source + location	Materials costs/prototype costs	Salt concentration/evaporation performance	Pollutants	Distilled water production rate	Durability test	Stability test	Ref
			magnitude lower than that of before the desalination process EE: 71.1% (15.5% NaCl)				desalination for 5 days	
Dual phases Mo <sub>2</sub> N/MoN nanorambutans	Artificial sea water	-	Salts (Na <sup>+</sup> , K <sup>+</sup> , Mg <sup>2+</sup> , Ca <sup>2+</sup> ) ER:1.70, EE:93	-	-	ER: of 1.66 kg m <sup>-2</sup> h <sup>-1</sup> , 91% efficiency after one week usage for 20 cycles, 3 h/cycle	-	[52]
Oxygen-defected molybdenum oxides hierarchical nanostructure	Artificial sea water	-	Na <sup>+</sup> , K <sup>+</sup> , Mg <sup>2+</sup> , Ca <sup>2+</sup> Indoor ER:1.050 kg m <sup>-2</sup> h <sup>-1</sup> Natural solar: 0.28 L m <sup>-2</sup> h <sup>-1</sup> /0.4 sun (8 h) 0.44 L m <sup>-2</sup> h <sup>-1</sup> /0.6 sun (8 h)	-	-	ER: 1.229 over 10 cycles	-	[75]
MoS <sub>2</sub> /C-polyurethane composite	Artificial sea water	≈\$0.93 in <sup>-3</sup>	-	Mercury Reduced from 200 ppm to 2 ppm Nickel Reduced, from 27 ppm to 1 ppm	-	-	It could be regenerated by optimizing the reduction-volatilization approach	[41]
MoS <sub>2</sub> on cotton cloth	Artificial sea water	-	Na <sup>+</sup> , K <sup>+</sup> , Mg <sup>2+</sup> , Ca <sup>2+</sup> ER: 1.3 kg m <sup>-2</sup> h <sup>-1</sup> for 4 h	-	-	Stable performance for 32 cycles (1 h/cycle) Stable after 1 M NaCl treatment	Stable after 1 M NaCl treatment	[128]
MoS <sub>2</sub>	East China Sea	-	Cations: Na <sup>+</sup> , K <sup>+</sup> , Ca <sup>2+</sup> , and Mg <sup>2+</sup> and anions: Cl <sup>-</sup> , Br <sup>-</sup> , NO <sub>3</sub> <sup>-</sup> and SO <sub>4</sub> <sup>2-</sup> Salts conc reduced from 0.032 to 3.56 mg L <sup>-1</sup>	Microp: Nitrobenzene, carbamazepine, and naproxen reduced from 400, 472.5 and 460.5 µg L <sup>-1</sup> to 276.7, 153.5 and 148.2 µg L <sup>-1</sup> after 4 h	-	Stable ER for 23 cycles within 210 days/2 sun	-	[97]
WC nanoarray on carbon fiber paper	Artificial sea water	-	3.5% NaCl ER:2.4 Man-made sea water (1.06 ± 0.10 kg m <sup>-2</sup> h <sup>-1</sup> ) Natural sunlight	Heavy metals As, Cd, Pb Conc. reduced to (0.01, 0.17, 0.73 ppm) ER: 0.98 ± 0.18 (distilled sewage) Natural sunlight	-	With 3.5% NaCl stable ER: 1.1 kg m <sup>-2</sup> h <sup>-1</sup> for 100 cycle. 1 h/cycle under one sun	washing the sample after each hour's desalination to maintain high evaporation rate	[131]
3D honeycomb CuFeMnO <sub>4</sub>	Artificial sea water	-	Synthetic sea water ~1.21 kg m <sup>-2</sup> h <sup>-1</sup>	Organic dyes MB Yielding fresh water: 0.612 kg h <sup>-1</sup> m <sup>-2</sup> , Removal efficiency: ~99.18	-	Repeated photo-Fenton degradation for 10 cycles (20 min/cycle)	-	[137]
ZnO-Au on mixed cellulose ester membrane	Artificial sea water	-	-	Organic dyes RhB conc. reduced to 30% after 120-min	-	-	-	[134]
SnSe@SnO <sub>2</sub> core-shell nanocomposite	-	-	-	Organic dyes MO ER: 1.19 kg m <sup>-2</sup> h <sup>-1</sup> , Complete degradation in 40 min with rate of 0.0934	-	Stable performance >95% for 10 cycles (3 h/cycle)	-	[141]

EE: Evaporation efficiency, ER: Evaporation rate, Microp: Micro-pollutants, RhB: Rhodamine B, MO: Methyl Orange, MB: Methylene Blue

(iv) **Water transport and anti-salt crystallization feature.** Water transport and anti-salt crystallization play an essential role in regulating heat-to-vapor generations. Further studies of designing nano/microstructure semiconductors with regulated properties (e.g., porosity, thickness, and dimensions) are required to investigate further the material's capability for allowing fast vapor escape with anti-salt properties. Apart from that, designing a device, which acts as a water transporter without the need for external water transport pathways such as utilizing metal foam or biomass materials with semiconductor PTMs would be an

attractive research direction. Besides, using computational approaches are essential for understanding the mechanism of water evaporation and salt migrations.

(v) **Reusability and stability tests.** The stability and reusability of a diverse range of semiconductor PTMs should be further explored under harsh environments (acidic and basic conditions). The current review reveals that stability and reusability were not investigated enough. There are wide research gaps regarding practical approaches.

(vi) **Cost and analysis for practical applications.** To bring semiconductor devices into real-world applications, several criteria must be considered: (i) using a low-cost approach with high efficient semiconductor PTMs which possess excellent solar conversion efficiency; (ii) fabricating scalable and realistic large scale devices (area: 1 m<sup>2</sup>); (iii) stable outdoor SSG performance under natural sunlight with long-term reusability even under harsh environment, and; (iv) conducting techno-economic analysis to calculate the overall cost of the semiconductors SSG devices to guarantee its implementation in large scale, practical and real field applications. These future efforts will make the semiconductor PTMs devices as a potential solution to address water scarcity.

### Declaration of competing interest

The authors declare that they have no known competing financial interests or personal relationships that could have appeared to influence the work reported in this paper.

### Acknowledgments

Idris Ibrahim is grateful for the financial support from the Australian Government through the International Research Training Program (IRTP) Scholarship for his Ph.D. studies. D.H.S acknowledges the support of UTS Chancellor's Postdoctoral Research Fellowship scheme. L.T. appreciates the support from UTS CTWW internal fund. H.K.S expresses gratitude for the support by the Korea Environment Industry & Technology Institute (KEITI) through Industrial Facilities & Infrastructure Research Program, funded by Korea Ministry of Environment (MOE) (1485016424), and also from the Australian Research Council (ARC) support.

### References

- [1] M.M. Mekonnen, A.Y. Hoekstra, Four billion people facing severe water scarcity, *Sci. Adv.* 2 (2016), e1500323.
- [2] W.H. Organization, Health and Environment in Sustainable Development: Five Years after the Earth Summit, World Health Organization, 1997.
- [3] A. Politano, P. Argurio, G. Di Profio, V. Sanna, A. Cupolillo, S. Chakraborty, H. A. Arafat, E. Curcio, Photothermal membrane distillation for seawater desalination, *Adv. Mater.* 29 (2017) 1603504.
- [4] Z. Wang, T. Horseman, A.P. Straub, N.Y. Yip, D. Li, M. Elimelech, S. Lin, Pathways and challenges for efficient solar-thermal desalination, *Science advances*, 5 (2019) eaax0763.
- [5] W.D.P.I.N. IDA, 22, MS Excel spreadsheet, Media Analytics Ltd, in, Oxford, UK, 2010.
- [6] E. Drioli, E. Curcio, Membrane engineering for process intensification: a perspective, *Journal of Chemical Technology & Biotechnology: International Research in Process, Environmental & Clean Technology* 82 (2007) 223–227.
- [7] A. Alsbaeie, B.J. Smith, L. Xiao, Y. Ling, D.E. Helbling, W.R. Dichtel, Rapid removal of organic micropollutants from water by a porous β-cyclodextrin polymer, *Nature* 529 (2016) 190.
- [8] M. Gao, L. Zhu, C.K. Peh, G.W. Ho, Solar absorber material and system designs for photothermal water vaporization towards clean water and energy production, *Energy Environ. Sci.* 12 (2019) 841–864.
- [9] P. Zhang, J. Li, L. Lv, Y. Zhao, L. Qu, Vertically aligned graphene sheets membrane for highly efficient solar thermal generation of clean water, *ACS Nano* 11 (2017) 5087–5093.
- [10] P. Tao, G. Ni, C. Song, W. Shang, J. Wu, J. Zhu, G. Chen, T. Deng, Solar-driven interfacial evaporation, *Nat. Energy* 3 (2018) 1031–1041.
- [11] T. Oki, S. Kanai, Global hydrological cycles and world water resources, *science*, 313 (2006) 1068–1072.
- [12] H.M. Qiblawey, F. Banat, Solar thermal desalination technologies, *Desalination* 220 (2008) 633–644.
- [13] P. Wang, Emerging investigator series: the rise of nano-enabled photothermal materials for water evaporation and clean water production by sunlight, *Environmental Science: Nano* 5 (2018) 1078–1089.
- [14] S.F. Anis, R. Hashaikeh, N. Hilal, Functional materials in desalination: a review, *Desalination* 468 (2019) 114077.
- [15] C. Chen, Y. Kuang, L. Hu, Challenges and opportunities for solar evaporation, *Joule* 3 (2019) 683–718.
- [16] Y. Zhang, M. Sivakumar, S. Yang, K. Enever, M. Ramezanianpour, Application of solar energy in water treatment processes: a review, *Desalination* 428 (2018) 116–145.
- [17] A. Kabeel, S. El-Agouz, Review of researches and developments on solar stills, *Desalination* 276 (2011) 1–12.
- [18] A. Kaushal, Solar stills: a review, *Renew. Sust. Energ. Rev.* 14 (2010) 446–453.
- [19] P. Zhang, Q. Liao, H. Yao, Y. Huang, H. Cheng, L. Qu, Direct solar steam generation system for clean water production, *Energy Storage Materials* 18 (2019) 429–446.
- [20] C. Chen, Y. Li, J. Song, Z. Yang, Y. Kuang, E. Hitz, C. Jia, A. Gong, F. Jiang, J. Zhu, Highly flexible and efficient solar steam generation device, *Adv. Mater.* 29 (2017) 1701756.
- [21] X. Li, W. Xu, M. Tang, L. Zhou, B. Zhu, S. Zhu, J. Zhu, Graphene oxide-based efficient and scalable solar desalination under one sun with a confined 2D water path, *Proc. Natl. Acad. Sci.* 113 (2016) 13953–13958.
- [22] R. Li, L. Zhang, L. Shi, P. Wang, MXene Ti<sub>3</sub>C<sub>2</sub>: an effective 2D light-to-heat conversion material, *ACS Nano* 11 (2017) 3752–3759.
- [23] C. Zhang, H.Q. Liang, Z.K. Xu, Z. Wang, Harnessing solar-driven photothermal effect toward the water-energy nexus, *Advanced Science* 6 (2019) 1900883.
- [24] Y. Xia, Q. Hou, H. Jubaer, Y. Li, Y. Kang, S. Yuan, H. Liu, M.W. Woo, L. Zhang, L. Gao, Spatially isolating salt crystallisation from water evaporation for continuous solar steam generation and salt harvesting, *Energy Environ. Sci.* 12 (2019) 1840–1847.
- [25] L. Zhang, L. Mu, Q. Zhou, X. Hu, Solar-assisted fabrication of dimpled 2H-MoS<sub>2</sub> membrane for highly efficient water desalination, *Water Res.* 170 (2020) 115367.
- [26] D.H. Seo, S. Pineda, Y.C. Woo, M. Xie, A.T. Murdock, E.Y. Ang, Y. Jiao, M.J. Park, S.I. Lim, M. Lawn, Anti-fouling graphene-based membranes for effective water desalination, *Nat. Commun.* 9 (2018) 1–12.
- [27] Y. Dong, L. Ma, C.Y. Tang, F. Yang, X. Quan, D. Jassby, M.J. Zaworotko, M. D. Guiver, Stable superhydrophobic ceramic-based carbon nanotube composite desalination membranes, *Nano Lett.* 18 (2018) 5514–5521.
- [28] Y. Shao, Z. Jiang, Y. Zhang, T. Wang, P. Zhao, Z. Zhang, J. Yuan, H. Wang, All-poly (ionic liquid) membrane-derived porous carbon membranes: scalable synthesis and application for photothermal conversion in seawater desalination, *ACS Nano* 12 (2018) 11704–11710.
- [29] C.-N. Yeh, K. Raidongia, J. Shao, Q.-H. Yang, J. Huang, On the origin of the stability of graphene oxide membranes in water, *Nat. Chem.* 7 (2015) 166.
- [30] C.-H. Lai, M.-Y. Lu, L.-J. Chen, Metal sulfide nanostructures: synthesis, properties and applications in energy conversion and storage, *J. Mater. Chem.* 22 (2012) 19–30.
- [31] Y. Shi, R. Li, Y. Jin, S. Zhuo, L. Shi, J. Chang, S. Hong, K.-C. Ng, P. Wang, A 3D photothermal structure toward improved energy efficiency in solar steam generation, *Joule* 2 (2018) 1171–1186.
- [32] T.F. Chala, C.-M. Wu, M.-H. Chou, Z.-L. Guo, Melt electrospun reduced tungsten oxide/polylactic acid fiber membranes as a photothermal material for light-driven interfacial water evaporation, *ACS Appl. Mater. Interfaces* 10 (2018) 28955–28962.
- [33] L. Zhu, M. Gao, C.K.N. Peh, G.W. Ho, Recent progress in solar-driven interfacial water evaporation: advanced designs and applications, *Nano Energy* 57 (2019) 507–518.
- [34] X. Wu, G.Y. Chen, G. Owens, D. Chu, H. Xu, Photothermal materials: a key platform enabling highly efficient water evaporation driven by solar energy, *Materials Today Energy* 12 (2019) 277–296.
- [35] F. Tao, M. Green, A.V. Garcia, T. Xiao, A.T. Van Tran, Y. Zhang, Y. Yin, X. Chen, Recent progress of nanostructured interfacial solar vapor generators, *Appl. Mater. Today* 17 (2019) 45–84.
- [36] G. Liu, J. Xu, K. Wang, Solar water evaporation by black photothermal sheets, *Nano Energy* 41 (2017) 269–284.
- [37] A.H. Elsheikh, S.W. Sharshir, M.K.A. Ali, J. Shaibo, E.M. Edreis, T. Abdelhamid, C. Du, Z. Haizou, Thin film technology for solar steam generation: a new dawn, *Sol. Energy* 177 (2019) 561–575.
- [38] J. Liang, H. Liu, J. Yu, L. Zhou, J. Zhu, Plasmon-enhanced solar vapor generation, *Nanophotonics* 8 (2019) 771–786.
- [39] X. Li, B. Zhu, J. Zhu, Graphene oxide based materials for desalination, *Carbon* 146 (2019) 320–328.
- [40] Y. Xu, J. Ma, Y. Han, J. Zhang, F. Cui, Y. Zhao, X. Li, W. Wang, Multifunctional CuO nanowire mesh for highly efficient solar evaporation and water purification, *ACS Sustain. Chem. Eng.* 7 (2019) 5476–5485.
- [41] W. Li, M.C. Tekell, Y. Huang, K. Bertelsmann, M. Lau, D. Fan, Synergistic high-rate solar steaming and mercury removal with MoS<sub>2</sub>/C@ polyurethane composite sponges, *Adv. Energy Mater.* 8 (2018) 1802108.
- [42] M. Shang, N. Li, S. Zhang, T. Zhao, C. Zhang, C. Liu, H. Li, Z. Wang, Full-spectrum solar-to-heat conversion membrane with interfacial plasmonic heating ability for high-efficiency desalination of seawater, *ACS Applied Energy Materials* 1 (2017) 56–61.
- [43] A. Polman, Solar steam nanobubbles, *ACS Nano* 7 (2013) 15–18.
- [44] Y. Liu, S. Yu, R. Feng, A. Bernard, Y. Liu, Y. Zhang, H. Duan, W. Shang, P. Tao, C. Song, A bioinspired, reusable, paper-based system for high-performance large-scale evaporation, *Adv. Mater.* 27 (2015) 2768–2774.
- [45] Y. Long, S. Huang, H. Yi, J. Chen, J. Wu, Q. Liao, H. Liang, H. Cui, S. Ruan, Y.-J. Zeng, Carrot-inspired solar thermal evaporator, *J. Mater. Chem. A* 7 (2019) 26911–26916.
- [46] P. Sun, W. Zhang, I. Zada, Y. Zhang, J. Gu, Q. Liu, H. Su, D. Pantelic, B. Jelenkovic, D. Zhang, 3D-structured carbonized sunflower heads for improved energy efficiency in solar steam generation, *ACS Appl. Mater. Interfaces* 12 (2019) 2171–2179.
- [47] Y. Bian, Q. Du, K. Tang, Y. Shen, L. Hao, D. Zhou, X. Wang, Z. Xu, H. Zhang, L. Zhao, Carbonized bamboos as excellent 3D solar vapor-generation devices, *Advanced Materials Technologies* 4 (2019) 1800593.

- [48] Y. Wang, X. Wu, T. Gao, Y. Lu, X. Yang, G.Y. Chen, G. Owens, H. Xu, Same materials, bigger output: a reversibly transformable 2D-3D photothermal evaporator for highly efficient solar steam generation, *Nano Energy* 105477 (2020).
- [49] T. Wu, H. Li, M. Xie, S. Shen, W. Wang, M. Zhao, X. Mo, Y. Xia, Incorporation of gold nanocages into electrospun nanofibers for efficient water evaporation through photothermal heating, *Materials Today Energy* 12 (2019) 129–135.
- [50] J. Zhou, Y. Gu, P. Liu, P. Wang, L. Miao, J. Liu, A. Wei, X. Mu, J. Li, J. Zhu, Development and evolution of the system structure for highly efficient solar steam generation from zero to three dimensions, *Adv. Funct. Mater.* 29 (2019) 1903255.
- [51] Y.-S. Jun, X. Wu, D. Ghim, Q. Jiang, S. Cao, S. Singamaneni, Photothermal membrane water treatment for two worlds, *Acc. Chem. Res.* 52 (5) (2019) 1215–1225.
- [52] L. Zhu, L. Sun, H. Zhang, D. Yu, H. Aslan, J. Zhao, Z. Li, M. Yu, F. Besenbacher, Y. Sun, Dual-phase molybdenum nitride nanorambutans for solar steam generation under one sun illumination, *Nano Energy* 57 (2019) 842–850.
- [53] C.A. Guemard, The sun's total and spectral irradiance for solar energy applications and solar radiation models, *Sol. Energy* 76 (2004) 423–453.
- [54] Y. Lin, H. Xu, X. Shan, Y. Di, A. Zhao, Y. Hu, Z. Gan, Solar steam generation based on the photothermal effect: from designs to applications, and beyond, *J. Mater. Chem. A* 7 (2019) 19203–19227.
- [55] F. Tao, Y. Zhang, S. Cao, K. Yin, X. Chang, Y. Lei, R. Fan, L. Dong, Y. Yin, X. Chen, CuS nanoflowers/semipermeable collodion membrane composite for high-efficiency solar vapor generation, *Materials Today Energy* 9 (2018) 285–294.
- [56] Y. Zhao, H. Pan, Y. Lou, X. Qiu, J. Zhu, C. Burda, Plasmonic Cu<sub>2-x</sub>S nanocrystals: optical and structural properties of copper-deficient copper (I) sulfides, *J. Am. Chem. Soc.* 131 (2009) 4253–4261.
- [57] C. Coughlan, M. Ibanez, O. Dobrozhan, A. Singh, A. Cabot, K.M. Ryan, Compound copper chalcogenide nanocrystals, *Chem. Rev.* 117 (2017) 5865–6109.
- [58] C. Zhang, C. Yan, Z. Xue, W. Yu, Y. Xie, T. Wang, Shape-controlled synthesis of high-quality Cu<sub>2</sub>S<sub>4</sub> nanocrystals for efficient light-induced water evaporation, *Small* 12 (2016) 5320–5328.
- [59] K. Sivula, R. Van De Krol, Semiconducting materials for photoelectrochemical energy conversion, *Nature Reviews Materials* 1 (2016) 15010.
- [60] C. Mu, Y. Song, K. Deng, S. Lin, Y. Bi, F. Scarpa, D. Crouse, High solar desalination efficiency achieved with 3D Cu<sub>2</sub>ZnSnS<sub>4</sub> nanosheet-assembled membranes, *Advanced Sustainable Systems* 1 (2017) 1700064.
- [61] Q. Guo, H.W. Hillhouse, R. Agrawal, Synthesis of Cu<sub>2</sub>ZnSnS<sub>4</sub> nanocrystal ink and its use for solar cells, *J. Am. Chem. Soc.* 131 (2009) 11672–11673.
- [62] J. Zhang, Y. Yang, J. Zhao, Z. Dai, W. Liu, C. Chen, S. Gao, D. Golosov, S. Zavadskis, S. Melnikov, Shape tailored Cu<sub>2</sub>ZnSnS<sub>4</sub> nanosheet aggregates for high efficiency solar desalination, *Mater. Res. Bull.* 110529 (2019).
- [63] Y. Hirate, H. Tampo, S. Minoura, H. Kadouaki, A. Nakane, K.M. Kim, H. Shibata, S. Niki, H. Fujiwara, Dielectric functions of Cu<sub>2</sub>ZnSnSe<sub>4</sub> and Cu<sub>2</sub>SnSe<sub>3</sub> semiconductors, *J. Appl. Phys.* 117 (2015), 015702.
- [64] Y. Yang, W. Que, J. Zhao, Y. Han, M. Ju, X. Yin, Membrane assembled from anti-fouling copper-zinc-tin-selenide nanocarambolas for solar-driven interfacial water evaporation, *Chem. Eng. J.* 373 (2019) 955–962.
- [65] Z. Li, M. Zheng, N. Wei, Y. Lin, W. Chu, R. Xu, H. Wang, J. Tian, H. Cui, Broadband-absorbing WO<sub>3-x</sub> nanorod-decorated wood evaporator for highly efficient solar-driven interfacial steam generation, *Sol. Energy Mater. Sol. Cells* 205 (2020) 110254.
- [66] C. Di Valentin, G. Pacchioni, Spectroscopic properties of doped and defective semiconducting oxides from hybrid density functional calculations, *Acc. Chem. Res.* 47 (2014) 3233–3241.
- [67] C.J. DeSantis, M.J. McClain, N.J. Halas, Walking the walk: a giant step toward sustainable plasmonics, *ACS Nano* 10 (2016) 9772–9775.
- [68] S. Cong, F. Geng, Z. Zhao, Tungsten oxide materials for optoelectronic applications, *Adv. Mater.* 28 (2016) 10518–10528.
- [69] D. Ding, W. Huang, C. Song, M. Yan, C. Guo, S. Liu, Non-stoichiometric MoO<sub>3-x</sub> quantum dots as a light-harvesting material for interfacial water evaporation, *Chem. Commun.* 53 (2017) 6744–6747.
- [70] A. Dey, Semiconductor metal oxide gas sensors: a review, *Mater. Sci. Eng. B* 229 (2018) 206–217.
- [71] M. Saenger, T. Höing, B.W. Robertson, R. Billa, T. Hofmann, E. Schubert, M. Schubert, Polaron and phonon properties in proton intercalated amorphous tungsten oxide thin films, *Phys. Rev. B* 78 (2008) 245205.
- [72] L. Sun, Z. Li, R. Su, Y. Wang, Z. Li, B. Du, Y. Sun, P. Guan, F. Besenbacher, M. Yu, Phase-transition induced conversion into a photothermal material: quasi-metallic WO<sub>2.9</sub> nanorods for solar water evaporation and anticancer photothermal therapy, *Angew. Chem. Int. Ed.* 57 (2018) 10666–10671.
- [73] Z. Fang, S. Jiao, B. Wang, W. Yin, G. Pang, A flexible, self-floating composite for efficient water evaporation, *Global Challenges* 3 (2019) 1800085.
- [74] Y. Chang, Z. Wang, Y.-e. Shi, X. Ma, L. Ma, Y. Zhang, J. Zhan, Hydrophobic W<sub>18</sub>O<sub>49</sub> mesocrystal on hydrophilic PTFE membrane as an efficient solar steam generation device under one sun, *J. Mater. Chem. A* 6 (2018) 10939–10946.
- [75] Q. Lu, Y. Yang, J. Feng, X. Wang, Oxygen-defected molybdenum oxides hierarchical nanostructure constructed by atomic-level thickness nanosheets as an efficient absorber for solar steam generation, *Solar RRL* 3 (2019) 1800277.
- [76] Y. Fang, X. Hu, W. Zhao, J. Pan, D. Wang, K. Bu, Y. Mao, S. Chu, P. Liu, T. Zhai, Structural determination and nonlinear optical properties of new 1T'''-type MoS<sub>2</sub> compound, *J. Am. Chem. Soc.* 141 (2019) 790–793.
- [77] S.N. Shirodkar, U.V. Waghmare, Emergence of ferroelectricity at a metal-semiconductor transition in a 1 T monolayer of MoS<sub>2</sub>, *Phys. Rev. Lett.* 112 (2014) 157601.
- [78] E. Bruyer, D. Di Sante, P. Barone, A. Stroppa, M.-H. Whangbo, S. Picozzi, Possibility of combining ferroelectricity and Rashba-like spin splitting in monolayers of the 1 T-type transition-metal dichalcogenides MX<sub>2</sub> (M=Mo, W; X=S, Se, Te), *Phys. Rev. B* 94 (2016) 195402.
- [79] S. Liu, T.H. Zeng, M. Hofmann, E. Burcombe, J. Wei, R. Jiang, J. Kong, Y. Chen, Antibacterial activity of graphite, graphite oxide, graphene oxide, and reduced graphene oxide: membrane and oxidative stress, *ACS Nano* 5 (2011) 6971–6980.
- [80] X. Wang, N.D. Mansukhani, L.M. Guiney, Z. Ji, C.H. Chang, M. Wang, Y.P. Liao, T. B. Song, B. Sun, R. Li, Differences in the toxicological potential of 2D versus aggregated molybdenum disulfide in the lung, *Small* 11 (2015) 5079–5087.
- [81] W.Z. Teo, E.L.K. Chng, Z. Sofer, M. Pumera, Cytotoxicity of exfoliated transition-metal dichalcogenides (MoS<sub>2</sub>, WS<sub>2</sub>, and WSe<sub>2</sub>) is lower than that of graphene and its analogues, *Chem. Eur. J.* 20 (2014) 9627–9632.
- [82] D. Ghim, Q. Jiang, S. Cao, S. Singamaneni, Y.-S. Jun, Mechanically interlocked 1T/2H phases of MoS<sub>2</sub> nanosheets for solar thermal water purification, *Nano Energy* 53 (2018) 949–957.
- [83] P. Xiong, B. Sun, N. Sakai, R. Ma, T. Sasaki, S. Wang, J. Zhang, G. Wang, 2D superlattices for efficient energy storage and conversion, *Adv. Mater.* 1902654 (2019).
- [84] S. Cui, Z. Wen, X. Huang, J. Chang, J. Chen, Stabilizing MoS<sub>2</sub> nanosheets through SnO<sub>2</sub> nanocrystal decoration for high-performance gas sensing in air, *Small* 11 (2015) 2305–2313.
- [85] J. Mann, Q. Ma, P.M. Odenthal, M. Isarraraz, D. Le, E. Preciado, D. Barroso, K. Yamaguchi, G. von Son Palacio, A. Nguyen, 2-Dimensional transition metal dichalcogenides with tunable direct band gaps: MoS<sub>2(1-x)Se<sub>2x</sub></sub> monolayers, *Adv. Mater.* 26 (2014) 1399–1404.
- [86] M. Naguib, M. Kurtoglu, V. Presser, J. Lu, J. Niu, M. Heon, L. Hultman, Y. Gogotsi, M.W. Barsoum, Two-dimensional nanocrystals produced by exfoliation of Ti<sub>3</sub>AlC<sub>2</sub>, *Adv. Mater.* 23 (2011) 4248–4253.
- [87] K. Li, T.H. Chang, Z. Li, H. Yang, F. Fu, T. Li, J.S. Ho, P.Y. Chen, Biomimetic MXene textures with enhanced light-to-heat conversion for solar steam generation and wearable thermal management, *Adv. Energy Mater.* 9 (2019) 1901687.
- [88] J. Chen, Y. Zhou, R. Li, X. Wang, G.Z. Chen, Highly-dispersed nickel nanoparticles decorated titanium dioxide nanotube array for enhanced solar light absorption, *Appl. Surf. Sci.* 464 (2019) 716–724.
- [89] M. Wang, M. Ye, J. Icozzetta, C. Lin, Z. Lin, Plasmon-mediated solar energy conversion via photocatalysis in noble metal/semiconductor composites, *Advanced Science* 3 (2016) 1600024.
- [90] H. Li, Y. He, Z. Liu, Y. Huang, B. Jiang, Synchronous steam generation and heat collection in a broadband Ag@TiO<sub>2</sub> core-shell nanoparticle-based receiver, *Appl. Therm. Eng.* 121 (2017) 617–627.
- [91] J. Huang, Y. He, L. Wang, Y. Huang, B. Jiang, Bifunctional Au@TiO<sub>2</sub> core-shell nanoparticle films for clean water generation by photocatalysis and solar evaporation, *Energy Convers. Manag.* 132 (2017) 452–459.
- [92] D. Wang, S.C. Pillai, S.-H. Ho, J. Zeng, Y. Li, D.D. Dionysiou, Plasmonic-based nanomaterials for environmental remediation, *Appl. Catal. B Environ.* 237 (2018) 721–741.
- [93] L. Yi, D. Qi, P. Shao, C. Lei, Y. Hou, P. Cai, G. Wang, X. Chen, Z. Wen, Hollow black TiAlO<sub>x</sub> nanocomposites for solar thermal desalination, *Nanoscale* 11 (2019) 9958–9968.
- [94] N. Wu, Plasmonic metal-semiconductor photocatalysts and photoelectrochemical cells: a review, *Nanoscale* 10 (2018) 2679–2696.
- [95] J. Wang, Y. Li, L. Deng, N. Wei, Y. Weng, S. Dong, D. Qi, J. Qiu, X. Chen, T. Wu, High-performance photothermal conversion of narrow-bandgap Ti<sub>2</sub>O<sub>3</sub> nanoparticles, *Adv. Mater.* 29 (2017) 1603730.
- [96] F. Tao, Y. Zhang, K. Yin, S. Cao, X. Chang, Y. Lei, D.S. Wang, R. Fan, L. Dong, Y. Yin, Copper sulfide-based plasmonic photothermal membrane for high-efficiency solar vapor generation, *ACS Appl. Mater. Interfaces* 10 (2018) 35154–35163.
- [97] R. Chen, X. Wang, Q. Gan, T. Zhang, K. Zhu, M. Ye, A bifunctional MoS<sub>2</sub>-based solar evaporator for both efficient water evaporation and clean freshwater collection, *J. Mater. Chem. A* 7 (2019) 11177–11185.
- [98] X. Yang, Y. Yang, L. Fu, M. Zou, Z. Li, A. Cao, Q. Yuan, An ultrathin flexible 2D membrane based on single-walled nanotube-MoS<sub>2</sub> hybrid film for high-performance solar steam generation, *Adv. Funct. Mater.* 28 (2018) 1704505.
- [99] J. Yao, Z. Zheng, G. Yang, Layered tin monoselenide as advanced photothermal conversion materials for efficient solar energy-driven water evaporation, *Nanoscale* 10 (2018) 2876–2886.
- [100] H. Ghasemi, G. Ni, A.M. Marconnet, J. Loomis, S. Yerci, N. Miljkovic, G. Chen, Solar steam generation by heat localization, *Nat. Commun.* 5 (2014) 4449.
- [101] T. Li, Q. Fang, X. Xi, Y. Chen, F. Liu, Ultra-robust carbon fibers for multi-media purification via solar-evaporation, *J. Mater. Chem. A* 7 (2019) 586–593.
- [102] J. Zhao, Y. Yang, C. Yang, Y. Tian, Y. Han, J. Liu, X. Yin, W. Que, A hydrophobic surface enabled salt-blocking 2D Ti<sub>3</sub>C<sub>2</sub> MXene membrane for efficient and stable solar desalination, *J. Mater. Chem. A* 6 (2018) 16196–16204.
- [103] H. Liu, C. Chen, H. Wen, R. Guo, N.A. Williams, B. Wang, F. Chen, L. Hu, Narrow bandgap semiconductor decorated wood membrane for high-efficiency solar-assisted water purification, *J. Mater. Chem. A* 6 (2018) 18839–18846.
- [104] D. Guo, X. Yang, Highly efficient solar steam generation of low cost TiN/bio-carbon foam, *Science China Materials* 62 (2019) 711–718.
- [105] W. Huang, P. Su, Y. Cao, C. Li, D. Chen, X. Tian, Y. Su, B. Qiao, J. Tu, X. Wang, Three-dimensional hierarchical Cu<sub>x</sub>S-based evaporator for high-efficiency multifunctional solar distillation, *Nano Energy* 69 (2020) 104465.

- [106] X. Wang, Y. Liu, R. Feng, Y. Zhang, C. Chang, B. Fu, T. Luan, P. Tao, W. Shang, J. Wu, Solar-driven high-temperature steam generation at ambient pressure, *Progress in Natural Science: Materials International* 29 (2019) 10–15.
- [107] S. Cao, Q. Jiang, X. Wu, D. Ghimi, H.G. Derami, P.-I. Chou, Y.-S. Jun, S. Singamaneni, Advances in solar evaporator materials for freshwater generation, *J. Mater. Chem. A* 7 (2019) 24092–24123.
- [108] X. Zhao, X.-J. Zha, J.-H. Pu, L. Bai, R.-Y. Bao, Z.-Y. Liu, M.-B. Yang, W. Yang, Macroporous three-dimensional MXene architectures for highly efficient solar steam generation, *J. Mater. Chem. A* 7 (2019) 10446–10455.
- [109] Y. Yang, H. Zhao, Z. Yin, J. Zhao, X. Yin, N. Li, D. Yin, Y. Li, B. Lei, Y. Du, A general salt-resistant hydrophilic/hydrophobic nanoporous double layer design for efficient and stable solar water evaporation distillation, *Materials Horizons* 5 (2018) 1143–1150.
- [110] Z. Guo, X. Ming, G. Wang, B. Hou, X. Liu, T. Mei, J. Li, J. Wang, X. Wang, Super-hydrophilic copper sulfide films as light absorbers for efficient solar steam generation under one sun illumination, *Semicond. Sci. Technol.* 33 (2018), 025008.
- [111] L. Yi, S. Ci, S. Luo, P. Shao, Y. Hou, Z. Wen, Scalable and low-cost synthesis of black amorphous Al-Ti-O nanostructure for high-efficient photothermal desalination, *Nano Energy* 41 (2017) 600–608.
- [112] X. Wu, M.E. Robson, J.L. Phelps, J.S. Tan, B. Shao, G. Owens, H. Xu, A flexible photothermal cotton-CuS nanocage-agarose aerogel towards portable solar steam generation, *Nano Energy* 56 (2019) 708–715.
- [113] Y. Zeng, J. Yao, B.A. Horri, K. Wang, Y. Wu, D. Li, H. Wang, Solar evaporation enhancement using floating light-absorbing magnetic particles, *Energy Environ. Sci.* 4 (2011) 4074–4078.
- [114] J. Wang, Z. Liu, X. Dong, C.-E. Hsiung, Y. Zhu, L. Liu, Y. Han, Microporous cokes formed in zeolite catalysts enable efficient solar evaporation, *J. Mater. Chem. A* 5 (2017) 6860–6865.
- [115] S. He, C. Chen, Y. Kuang, R. Mi, Y. Liu, Y. Pei, W. Kong, W. Gan, H. Xie, E. Hitz, Nature-inspired salt resistant bimodal porous solar evaporator for efficient and stable water desalination, *Energy Environ. Sci.* 12 (2019) 1558–1567.
- [116] M. Elimelech, W.A. Phillip, The future of seawater desalination: energy, technology, and the environment, *science*, 333 (2011) 712–717.
- [117] C. Song, T. Li, W. Guo, Y. Gao, C. Yang, Q. Zhang, D. An, W. Huang, M. Yan, C. Guo, Hydrophobic Cu<sub>12</sub>Sb<sub>4</sub>S<sub>13</sub>-deposited photothermal film for interfacial water evaporation and thermal antibacterial activity, *New J. Chem.* 42 (2018) 3175–3179.
- [118] R. Chen, K. Zhu, Q. Gan, Y. Yu, T. Zhang, X. Liu, M. Ye, Y. Yin, Interfacial solar heating by self-assembled Fe<sub>3</sub>O<sub>4</sub>@C film for steam generation, *Materials Chemistry Frontiers* 1 (2017) 2620–2626.
- [119] R. Chen, Z. Wu, T. Zhang, T. Yu, M. Ye, Magnetically recyclable self-assembled thin films for highly efficient water evaporation by interfacial solar heating, *RSC Adv.* 7 (2017) 19849–19855.
- [120] L. Zhao, Q. Yang, W. Guo, H. Liu, T. Ma, F. Qu, Co<sub>2.67</sub>S<sub>4</sub>-based photothermal membrane with high mechanical properties for efficient solar water evaporation and photothermal antibacterial applications, *ACS Appl. Mater. Interfaces* 11 (2019) 20820–20827.
- [121] M. Ye, J. Jia, Z. Wu, C. Qian, R. Chen, P.G. O'Brien, W. Sun, Y. Dong, G.A.J.A.E.M. Ozin, Synthesis of black TiO<sub>x</sub> nanoparticles by Mg reduction of TiO<sub>2</sub> nanocrystals and their application for solar water evaporation, *Adv. Energy Mater.* 7 (2017) 1601811.
- [122] M. Ye, J. Jia, Z. Wu, C. Qian, R. Chen, P.G. O'Brien, W. Sun, Y. Dong, G.A.J.A.E.M. Ozin, Synthesis of black TiO<sub>x</sub> nanoparticles by Mg reduction of TiO<sub>2</sub> nanocrystals and their application for solar water evaporation, 7 (2017) 1601811.
- [123] Y. Guo, H. Lu, F. Zhao, X. Zhou, W. Shi, G. Yu, Biomass-derived hybrid hydrogel evaporators for cost-effective solar water purification, *Adv. Mater.* 32 (2020) 1907061.
- [124] X. Zhang, X. Wang, W.D. Wu, X.D. Chen, Z. Wu, Self-floating monodisperse microparticles with a nano-engineered surface composition and structure for highly efficient solar-driven water evaporation, *J. Mater. Chem. A* 7 (2019) 6963–6971.
- [125] J. Xu, F. Xu, M. Qian, Z. Li, P. Sun, Z. Hong, F. Huang, Copper nanodot-embedded graphene urchins of nearly full-spectrum solar absorption and extraordinary solar desalination, *Nano Energy* 53 (2018) 425–431.
- [126] Y. Shi, R. Li, L. Shi, E. Ahmed, Y. Jin, P. Wang, A robust CuCr<sub>2</sub>O<sub>4</sub>/SiO<sub>2</sub> composite photothermal material with underwater black property and extremely high thermal stability for solar-driven water evaporation, *Advanced Sustainable Systems* 2 (2018) 1700145.
- [127] N. Li, D. Yin, L. Xu, H. Zhao, Z. Liu, Y. Du, High-quality ultralong copper sulphide nanowires for promising applications in high efficiency solar water evaporation, *Materials Chemistry Frontiers* 3 (2019) 394–398.
- [128] Z. Guo, G. Wang, X. Ming, T. Mei, J. Wang, J. Li, J. Qian, X. Wang, PEGylated self-growth Mo<sub>2</sub> on a cotton cloth substrate for high-efficiency solar energy utilization, *ACS Appl. Mater. Interfaces* 10 (2018) 24583–24589.
- [129] L. Sun, Z. Li, R. Su, Y. Wang, Z. Li, B. Du, Y. Sun, P. Guan, F. Besenbacher, M. Yu, Phase-transition induced conversion into a photothermal material: quasi-metallic WO<sub>2</sub>.9 nanorods for solar water evaporation and anticancer photothermal therapy, *Angew. Chem.* 130 (2018) 10826–10831.
- [130] X. Ming, A. Guo, G. Wang, X. Wang, Two-dimensional defective tungsten oxide nanosheets as high performance photo-absorbers for efficient solar steam generation, *Sol. Energy Mater. Sol. Cells* 185 (2018) 333–341.
- [131] N. Han, K. Liu, X. Zhang, M. Wang, P. Du, Z. Huang, D. Zhou, Q. Zhang, T. Gao, Y. Jia, Highly efficient and stable solar-powered desalination by tungsten carbide nanoarray film with sandwich wettability, *Science Bulletin* 64 (2019) 391–399.
- [132] D. Ding, W. Huang, C. Song, M. Yan, C. Guo, S. Liu, Non-stoichiometric MoO<sub>3-x</sub> quantum dots as a light-harvesting material for interfacial water evaporation, *Chem. Commun.* 53 (2017) 6744–6747.
- [133] M. Wang, P. Wang, J. Zhang, C. Li, Y. Jin, A ternary Pt/Au/TiO<sub>2</sub>-decorated plasmonic wood carbon for high-efficiency interfacial solar steam generation and photodegradation of tetracycline, *ChemSusChem* 12 (2019) 467–472.
- [134] X. Wang, Y. He, X. Liu, Synchronous steam generation and photodegradation for clean water generation based on localized solar energy harvesting, *Energy Convers. Manag.* 173 (2018) 158–166.
- [135] H. Liu, X. Zhang, Z. Hong, Z. Pu, Q. Yao, J. Shi, G. Yang, B. Mi, B. Yang, X. Liu, A bioinspired capillary-driven pump for solar vapor generation, *Nano Energy* 42 (2017) 115–121.
- [136] J. Huang, Y. He, M. Chen, X. Wang, Separating photo-thermal conversion and steam generation process for evaporation enhancement using a solar absorber, *Appl. Energy* 236 (2019) 244–252.
- [137] L. Shi, Y. Shi, S. Zhuo, C. Zhang, Y. Aldrees, S. Aleid, P. Wang, Multi-functional 3D honeycomb ceramic plate for clean water production by heterogeneous photo-Fenton reaction and solar-driven water evaporation, *Nano Energy* 60 (2019) 222–230.
- [138] P. Wang, Y. Gu, L. Miao, J. Zhou, H. Su, A. Wei, X. Mu, Y. Tian, J. Shi, H. Cai, Co<sub>3</sub>O<sub>4</sub> nanoforest/Ni foam as the interface heating sheet for the efficient solar-driven water evaporation under one sun, *Sustain. Mater. Technol.* 20 (2019), e00106.
- [139] Y. Liu, X. Wang, H. Wu, High-performance wastewater treatment based on reusable functional photo-absorbers, *Chem. Eng. J.* 309 (2017) 787–794.
- [140] D. Wu, D. Qu, W. Jiang, G. Chen, L. An, C. Zhuang, Z. Sun, Self-floating nanostructured Ni-NiO<sub>x</sub>/Ni foam for solar thermal water evaporation, *J. Mater. Chem. A* 7 (2019) 8485–8490.
- [141] Z. Li, L. Sun, Y. Liu, L. Zhu, D. Yu, Y. Wang, Y. Sun, M. Yu, SnSe@SnO<sub>2</sub> core-shell nanocomposite for synchronous photothermal–photocatalytic production of clean water, *Environmental Science: Nano* 6 (2019) 1507–1515.
- [142] C. Chang, P. Tao, B. Fu, J. Xu, C. Song, J. Wu, W. Shang, T. Deng, Three-dimensional porous solar-driven interfacial evaporator for high-efficiency steam generation under low solar flux, *ACS Omega* 4 (2019) 3546–3555.
- [143] H. Cheng, X. Liu, L. Zhang, B. Hou, F. Yu, Z. Shi, X. Wang, Self-floating Bi<sub>2</sub>S<sub>3</sub>/poly(vinylidene fluoride) composites on polyurethane sponges for efficient solar water purification, *Sol. Energy Mater. Sol. Cells* 203 (2019) 110127.
- [144] G. Ni, S.H. Zandavi, S.M. Javid, S.V. Boriskina, T.A. Cooper, G. Chen, A salt-rejecting floating solar still for low-cost desalination, *Energy Environ. Sci.* 11 (2018) 1510–1519.
- [145] F. Zhao, X. Zhou, Y. Shi, X. Qian, M. Alexander, X. Zhao, S. Mendez, R. Yang, L. Qu, G. Yu, Highly efficient solar vapour generation via hierarchically nanostructured gels, *Nat. Nanotechnol.* 13 (2018) 489–495.
- [146] M. Fujiwara, T. Imura, Photo induced membrane separation for water purification and desalination using azobenzene modified anodized alumina membranes, *ACS Nano* 9 (2015) 5705–5712.
- [147] W.W. Ngah, M.M. Hanafiah, Removal of heavy metal ions from wastewater by chemically modified plant wastes as adsorbents: a review, *Bioresour. Technol.* 99 (2008) 3935–3948.
- [148] C.E. Stephan, D.I. Mount, D.J. Hansen, J. Gentile, G.A. Chapman, W.A. Brungs, Guidelines for Deriving Numerical National Water Quality Criteria for the Protection of Aquatic Organisms and their Uses, US Environmental Protection Agency Washington, DC, 1985.
- [149] G. Zhu, J. Xu, W. Zhao, F. Huang, Constructing black titania with unique nanocage structure for solar desalination, *ACS Appl. Mater. Interfaces* 8 (2016) 31716–31721.